
Research Articles: Development/Plasticity/Repair

An Image-Based miRNA screen identifies miRNA-135s as regulators of CNS axon growth and regeneration by targeting Krüppel-like factor 4

Eljo Y. van Battum¹, Marieke G. Verhagen¹, Vamshidhar R. Vangoor¹, Yuki Fujita², Alwin A. H. A. Derijck¹, Eoghan O'Duibhir¹, Giuliano Giuliani¹, Thijs de Gunst³, Youri Adolfs¹, Daphne Lelieveld⁴, David Egan⁴, Roel Q.J. Schaapveld³, Toshihide Yamashita² and R. Jeroen Pasterkamp¹

¹Department of Translational Neuroscience, Brain Center Rudolf Magnus, University Medical Center Utrecht, Utrecht University, 3584 CG, Utrecht, The Netherlands

²Department of Molecular Neuroscience, Graduate School of Medicine, Osaka University, 2-2 Yamadaoka, Suita, Osaka 565-0871, Japan

³InterRNA Technologies B.V., Yalelaan 62, 3584 CM, Utrecht, The Netherlands

⁴Department of Cell Biology, Center for Molecular Medicine, University Medical Center Utrecht, Utrecht University, 3584 CX, Utrecht, The Netherlands

DOI: 10.1523/JNEUROSCI.0662-17.2017

Received: 9 March 2017

Revised: 24 October 2017

Accepted: 29 October 2017

Published: 1 December 2017

Author contributions: E.V.B., M.V., V.V., Y.F., A.D., E.O., G.G., and J.P. designed research; E.V.B., M.V., V.V., Y.F., A.D., E.O., G.G., Y.A., and T.Y. performed research; E.V.B., M.V., V.V., Y.F., A.D., E.O., G.G., Y.A., and J.P. analyzed data; T.d.G., D.L., D.E., and R.S. contributed unpublished reagents/analytic tools; J.P. wrote the paper.

Conflict of Interest: The authors declare no competing financial interests.

This work was financially supported by the Center for Translational Molecular Medicine (CTMM, project EMINENCE 01C-204), the Netherlands Organization for Health Research and Development (ZonMW-VIDI), the Netherlands Organization for Scientific Research (ALW-VICI), the Epilepsiefonds (WAR 12-08, 15-05), and the FP7-HEALTH-2013-INNOVATION-1 Collaborative project Epi-miRNA, all to R.J.P., and a Grant-in-Aid for Scientific Research (S) from the Japan Society for the Promotion of Science (25221309) to T.Y. Conflict of interest: R.Q.J.S. is a shareholder in InterRNA Technologies B.V., R.Q.J.S. and T.d.G. are stock option holders in InterRNA Technologies B.V. We thank Marina de Wit for technical assistance and members of the Pasterkamp laboratory for helpful discussions.

Corresponding author: Prof. R.J. Pasterkamp, Department of Translational Neuroscience, Brain Center Rudolf Magnus, University Medical Center Utrecht, Universiteitsweg 100, 3584 CG, Utrecht, The Netherlands. r.j.pasterkamp@umcutrecht.nl

Cite as: J. Neurosci ; 10.1523/JNEUROSCI.0662-17.2017

Alerts: Sign up at www.jneurosci.org/cgi/alerts to receive customized email alerts when the fully formatted version of this article is published.

Accepted manuscripts are peer-reviewed but have not been through the copyediting, formatting, or proofreading process.

1 **An Image-Based miRNA screen identifies miRNA-135s as regulators of CNS axon**
2 **growth and regeneration by targeting Krüppel-like factor 4**

3

4 Eljo Y. van Battum¹, Marieke G. Verhagen¹, Vamshidhar R. Vangoor¹, Yuki Fujita², Alwin A. H. A.
5 Derijck¹, Eoghan O'Duibhir¹, Giuliano Giuliani¹, Thijs de Gunst³, Youri Adolfs¹, Daphne Lelieveld⁴,
6 David Egan⁴, Roel Q.J. Schaapveld³, Toshihide Yamashita², and R. Jeroen Pasterkamp¹

7

8 ¹*Department of Translational Neuroscience, Brain Center Rudolf Magnus, University Medical Center Utrecht,*
9 *Utrecht University, 3584 CG, Utrecht, The Netherlands*
10 ²*Department of Molecular Neuroscience, Graduate School of Medicine, Osaka University, 2-2 Yamadaoka,*
11 *Suita, Osaka 565-0871, Japan*
12 ³*InteRNA Technologies B.V., Yalelaan 62, 3584 CM, Utrecht, The Netherlands*
13 ⁴*Department of Cell Biology, Center for Molecular Medicine, University Medical Center Utrecht, Utrecht*
14 *University, 3584 CX, Utrecht, The Netherlands*
15

16 **Abbreviated title:** miR-135-KLF4 in CNS axon growth and regeneration

17 **Corresponding author:** Prof. R.J. Pasterkamp, Department of Translational Neuroscience, Brain Center Rudolf
18 Magnus, University Medical Center Utrecht, Universiteitsweg 100, 3584 CG, Utrecht, The Netherlands.
19 r.j.pasterkamp@umcutrecht.nl

20

21 **Number of pages:** 57 **Number of Figures/Tables:** 8 (6 Figures, 2 Tables)

22 **Number of words in Abstract:** 203 **Introduction:** 505 **Discussion:** 1630

23

24 **Acknowledgements:** This work was financially supported by the Center for Translational Molecular Medicine
25 (CTMM, project EMINENCE 01C-204), the Netherlands Organization for Health Research and Development
26 (ZonMW-VIDI), the Netherlands Organization for Scientific Research (ALW-VICI), the Epilepsiefonds (WAR
27 12-08, 15-05), and the FP7-HEALTH-2013-INNOVATION-1 Collaborative project Epi-miRNA, all to R.J.P.,
28 and a Grant-in-Aid for Scientific Research (S) from the Japan Society for the Promotion of Science (25221309)
29 to T.Y. Conflict of interest: R.Q.J.S. is a shareholder in InteRNA Technologies B.V., R.Q.J.S. and T.d.G. are
30 stock option holders in InteRNA Technologies B.V. We thank Marina de Wit for technical assistance and
31 members of the Pasterkamp laboratory for helpful discussions.

32 **Abstract**

33

34 During embryonic development, axons extend over long distances to establish functional
35 connections. In contrast, axon regeneration in the adult mammalian central nervous system
36 (CNS) is limited, in part by a reduced intrinsic capacity for axon growth. Therefore, insight
37 into the intrinsic control of axon growth may provide new avenues for enhancing CNS
38 regeneration. Here, we performed one of the first miRNome-wide functional miRNA screens
39 to identify microRNAs (miRNAs) with robust effects on axon growth. High-content
40 screening identified miR-135a and miR-135b as potent stimulators of axon growth and
41 cortical neuron migration *in vitro* and *in vivo* in male and female mice. Intriguingly, both
42 these developmental effects of miR-135s relied, in part, on silencing of KLF4, a well-known
43 intrinsic inhibitor of axon growth and regeneration. These results prompted us to test the
44 effect of miR-135s on axon regeneration following injury. Our study shows that intravitreal
45 application of miR-135s facilitates retinal ganglion cell (RGC) axon regeneration following
46 optic nerve injury (ONI) in adult mice in part by repressing KLF4. In contrast, depletion of
47 miR-135s further reduced RGC axon regeneration. Together, these data identify a novel
48 neuronal role for miR-135s and the miR-135-KLF-4 pathway, and highlight the potential of
49 miRNAs as tools for enhancing CNS axon regeneration.

50 **Significance statement**

51

52 Axon regeneration in the adult mammalian central nervous system (CNS) is limited, in part
53 by a reduced intrinsic capacity for axon growth. Therefore, insight into the intrinsic control of
54 axon growth may provide new avenues for enhancing regeneration. By performing a
55 miRNome-wide functional screen, our studies identify miR-135s as stimulators of axon
56 growth and neuron migration, and show that intravitreal application of these miRNAs
57 facilitates CNS axon regeneration following nerve injury in adult mice. Intriguingly, these
58 developmental and regeneration-promoting effects rely, in part, on silencing of KLF4, a well-
59 known intrinsic inhibitor of axon regeneration. Our data identify a novel neuronal role for the
60 miR-135-KLF4 pathway and support the idea that miRNAs can be used for enhancing CNS
61 axon regeneration.

62 **Introduction**

63

64 During neural circuit development, newly born neurons grow their axons over long distances
65 to establish functional connections. This remarkable capacity for axon growth dramatically
66 reduces as the mammalian nervous system matures. While adult neurons that contribute their
67 axons to peripheral nerves display varying degrees of regrowth after trauma or injury, axonal
68 projections in the mammalian central nervous system (CNS) show limited capacity for
69 regeneration. This regenerative failure is caused by the presence of inhibitory factors at the
70 site of injury and a decrease in intrinsic growth ability of affected neurons (Baldwin and
71 Giger, 2015; He and Jin, 2016). One approach to promote CNS axon regeneration has
72 therefore been to target intrinsic factors that promote or inhibit axon growth, such as
73 Phosphate and tensin homologue (PTEN), Suppressor of cytokine signalling 3 (Socs3), or
74 Krüppel-like factors (KLFs) (He and Jin, 2016). These studies demonstrate that enhancing the
75 intrinsic growth ability of injured neurons induces robust axon regeneration and support the
76 idea that further knowledge of the intrinsic control of axon growth is needed for the design of
77 more effective therapeutic strategies for promoting CNS axon regeneration.

78 MicroRNAs (miRNAs) are small, non-coding RNAs that post-transcriptionally
79 regulate gene expression by controlling messenger RNA (mRNA) stability or translation
80 (Lagos-Quintana et al., 2001). MiRNAs are highly abundant in the nervous system and they
81 have been implicated in various aspects of neuron development and function including in
82 axon growth, guidance and branching (Baudet et al., 2013; Aksoy-Aksel et al., 2014).
83 However, the *in vivo* function(s) and downstream mRNA targets of many of the neuronally
84 expressed miRNAs remain unknown. The expression of miRNAs is strongly regulated
85 following nervous system injury and genetic inactivation of miRNA biogenesis hampers
86 peripheral nerve regeneration (e.g (Song et al., 2012; Wu et al., 2012; Zou et al., 2013;

87 Hancock et al., 2014; Phay et al., 2015; Li et al., 2016; Martirosyan et al., 2016)). In addition,
88 manipulation of miRNA expression in adult sensory neurons promotes peripheral nerve
89 regeneration (e.g. (Jiang et al., 2015; Gaudet et al., 2016; Hu et al., 2016)). However, whether
90 or not manipulation of miRNAs in injured CNS neurons also enhances CNS axon
91 regeneration in mammals, and if so, through which mRNA targets is unknown.

92 Here, we performed a genome-wide miRNA screen aimed at identifying functional
93 miRNAs with positive effects on axon growth. High content screening of more than one
94 thousand miRNAs in neuronal cells identified a novel role for miR-135b, and miR-135a, as
95 axon growth- and neuron migration-promoting factors. Further, our data show that intravitreal
96 application of miR-135s facilitates regeneration of retinal ganglion cell (RGC) axons
97 following optic nerve injury (ONI) in adult mice. In contrast, decreasing the availability of
98 miR-135s further inhibits RGC axon regeneration. The developmental and regeneration-
99 promoting effects of miR-135s both rely, in part, on silencing of KLF4, a well-known
100 intrinsic inhibitor of axon regeneration (Moore et al., 2009; Qin et al., 2013). Together, these
101 data identify novel neuronal functions for miR-135s and highlight the potential of applying
102 miRNAs to injured CNS neurons as an approach for facilitating CNS axon regeneration.

103 **Materials and Methods**

104

105 *Animals*

106 All animal use and care was carried out in accordance with institutional guidelines and
107 approved by the local ethical animal experimentation committee (DEC). C57Bl/6J mice
108 (RRID:IMSR_JAX:000664, male and female) were obtained from Charles River. When
109 timed-pregnant females were used, the morning on which a vaginal plug was detected was
110 considered embryonic day 0.5 (E0.5). For pups the day of birth was considered postnatal day
111 0 (P0).

112

113 *Lentiviral human whole miRnome library high content screen and hit confirmation*

114 SH-SY5Y cells, obtained from DSMZ (Acc 209, RRID:CVCL_0019), were grown in
115 DMEM-F12 (Gibco) + 10% FCS + L-Glutamine + penicillin/streptomycin and used between
116 passage 12 and 21. Cells were seeded in 96-wells plates using an automated cell-seeder
117 Multidrop Combi Reagent Dispenser (Thermo Scientific) at 6000 cells/well. One day after
118 seeding, cells were treated with 60 μ M retinoic acid and transduced with a lentiviral human
119 genome-wide miRNA library at on average 7.34×10^5 IFU/well (InterNA Technologies).
120 Each library plate was evaluated in triplicate. The lentiviral library contains 640 annotated
121 human miRNA genes (miRBase 12) and 400 candidate miRNAs from deep-sequencing
122 efforts and is based on the pCDH-CMV-MCS-EF1-Puro vector (No CD510B-1, System
123 Biosciences) (Poell et al., 2011). Systems Bioscience performed the lentiviral packaging and
124 the library had an average IFU/ml of 1.22×10^9 . The library was stored in 14 96-wells plates.
125 At 4 days *in vitro* (DIV), cells were fixed by addition of 1:1 8% paraformaldehyde in PBS
126 and blocked in 0.4% Triton-X100, 5% Goat Serum, 1% BSA, 1% glycin, and 0.1% lysin in
127 PBS. Cells were immunostained for β III-tubulin (1:3000, mouse monoclonal T8660, Sigma,

128 RRID:AB_477590) with an Alexa 488-conjugated secondary antibody (Invitrogen) and
129 counterstained with DAPI. Cells were automatically washed thoroughly by two washing
130 cycles with an AquaMax 2000 (Molecular Devices). Automated microscopy was carried out
131 using a Thermo ArrayScan VTI HCS Reader (Thermo Scientific) and morphological features
132 were extracted with the Cellomics Neuronal Profiling V3 Bioapplication algorithm (settings
133 can be found in Table 1). Raw data (.mdb files) were converted into Excel format using a
134 custom script (courtesy of Ronald van Kesteren, Vrije Universiteit Amsterdam). All wells
135 with a valid nucleus count below 100 were removed. Non-neuronal attributes and attributes
136 dependent on cell number were trimmed from the dataset. For all other attributes (as
137 described in Table 1) the plate median was calculated. Each attribute of each well was scored
138 binary (0 or 1), with a positive score (1) when deviating more than 2 times from the standard
139 deviation of the control median. The median of all miRNAs was used as control, assuming
140 that most miRNAs would not affect cell morphology. Triplicates of each plate were combined
141 and a well attribute was taken as ‘true’ when a minimum of 2 out of 3 plates scored positive.
142 This resulted in a final (cumulative) ‘hitscore’ which was used to rank the lentiviral clones
143 with effects on neuronal morphology.

144 For hit confirmation, SH-SY5Y cells were harvested by trypsinization, washed with
145 PBS and resuspended at 8×10^6 cells/ml in INB buffer (135 mM KCl, 0.2 mM CaCl_2 , 2 mM
146 MgCl_2 , 10 mM HEPES, 5 mM EGTA, pH 7.3). Then, cells were mixed with 20 pmol
147 miRIDIAN mimic (always the human (hsa) isoform, Dharmacon, ThermoScientific) and
148 electroporated with 3 120V pulses of 900 μs and 2 s pulse interval in a 1 mm gap size cuvet in
149 an ECM 830 square wave generator with PEP cuvette module (all BTX Harvard Apparatus).
150 In this way, over 98% of the cells are electroporated. Each electroporation was divided and
151 equally distributed over 4 wells of a 24-wells plate, leaving the outer left and right wells
152 without cells to take into account possible edge-well effects. One day post-electroporation,

153 cells were treated with 60 μ M retinoic acid to induce the development of neuron-like features.
154 Four days after electroporation, cells were fixed and immunostained as described above.
155 Analysis of morphological cell features was performed using the Cellomics software outlined
156 above.

157

158 *Locked nucleic acid (LNA) in situ hybridization*

159 E16.5 C57BL/6J mouse embryos were collected and decapitated. Brains were fixed in 4%
160 PFA in PBS and cryoprotected in 30% sucrose in PBS. Twenty μ m thick coronal brain
161 cryosections were made. LNA *in situ* hybridization was performed as previously described
162 (Kan et al., 2012). Briefly, sections were air-dried and post-fixed for 10 min in 4% PFA,
163 acetylated (10 min RT), treated with proteinase K (5 μ g/ml for 5 min at RT) and
164 prehybridized (1 h at RT, 30 min at 55°C) before incubation with 15 nM of LNA-containing,
165 double DIG-labeled miR-135a, miR-135b or control *in situ* probes (Exiqon) (2 h, at 55°C).
166 After hybridization, slides were washed in 0.2x SSC for 1 h at 55°C. Slides were blocked 1 h
167 with 10% FCS in PBS and incubated with anti-digoxigenin-AP Fab fragments (1:2500, Roche
168 Diagnostics) in blocking buffer ON at 4°C. After PBS washes, slides were incubated with
169 nitroblue and 5-bromo-4-chloro-3-indolyl phosphate (NBT/BCIP, Roche Diagnostics)
170 substrates for 2-20 h at RT. Staining was terminated by washing of the slides in PBS. Slides
171 were mounted in 90% glycerol in PBS. Sections stained with scrambled LNA-DIG probe
172 were devoid of specific staining.

173

174 *Quantitative PCR*

175 E14.5 and E16.5 C57BL/6 embryos, P0 and P10 pups, and adult mice were decapitated and
176 brains were removed. Hippocampi and cortices were dissected and frozen immediately on
177 dry-ice. Total RNA was isolated from at least 3 animals from 3 different litters using the

178 miRNeasy kit (Qiagen) according to manufacturer's protocol. In addition, total RNA was
179 isolated from primary hippocampal neurons from 3-4 coverslips out of 2 different cultures at
180 DIV 2, 7, 14, and 21. Furthermore, total RNA was isolated from retina 14 days after optic
181 nerve crush experiments and intravitreal injection of miRNA mimics (see paragraph
182 describing optic nerve injury experiments). RNA quantity was determined using Nanodrop
183 (Thermo Scientific) and equal amounts of each sample were used for first strand cDNA
184 synthesis using universal cDNA synthesis kit (Exiqon). Quantitative PCR reactions were run on
185 Quantstudio 6 flex Real-Time PCR system (Applied Biosystems) using microRNA LNATM
186 PCR primer sets and SYBR Green master mix (Exiqon). All samples were run in duplicates.
187 Ct values were determined using Quant studio real time pcr software v1.1. The expression
188 levels of different miRNAs were estimated by normalization to 5S rRNA, and the statistical
189 significance was analyzed with single factor ANOVA. $p < 0.05$ was evaluated as significant.

190

191 *Culturing and transfection of mouse hippocampal and cortical neurons*

192 Hippocampal and cortical cultures were generated as described previously (Van Battum et al.,
193 2014). In brief, P0-P1 C57BL/6 mouse pups were decapitated and brains were rapidly
194 removed in ice-cold dissection medium. Hippocampi or cortices were isolated, trypsinized
195 and dissociated into single cells. They were cultured in neurobasal medium supplemented
196 with B-27, L-glutamine, penicillin/streptomycin, and β -mercaptoethanol, on acid-washed,
197 poly-D-lysine (PDL, 20 $\mu\text{g}/\text{ml}$) and laminin (40 $\mu\text{g}/\text{ml}$)-coated glass coverslips at 37°C + 5%
198 CO₂ in 12-well plates. On DIV 1 neurons were co-transfected with 0.5 μg CAG-GFP vector
199 and 50 pmol miRIDIAN mimics for miR-135a, miR-135b, or control-1 mimic (also known as
200 Negative control-A, all obtained from Dharmacon) per well, or 0.5 μg miRNA H1-mCherry-
201 sponge vectors per well for miR-135a or miR-135b (Tebu-bio) using Lipofectamine 2000
202 (Invitrogen). For rescue experiments, a pCMV-KLF4-EGFP vector (Origene) was used. On

203 DIV4, neurons were fixed with 4% PFA and 4% sucrose in PBS. For immunocytochemistry,
204 neurons were incubated with rabbit anti-GFP (1:1000, A-11122, Invitrogen,
205 RRID:AB_221569) or rabbit-anti-RFP (1:1000, Rockland, RRID:AB_11182807) and mouse
206 anti- β III tubulin (1:3000, T8660, Sigma, RRID:AB_477590) dissolved in 3% normal horse
207 serum, 0.1% BSA and 0.1% triton-X100 in PBS. Images were taken using an Axioskop 2 EPI
208 fluorescent microscope (Zeiss). Longest neurites were traced semi-manually using the
209 NeuronJ plugin (RRID:SCR_002074) of ImageJ and sholl analysis was performed using
210 ImageJ software (RRID:SCR_003070). More than 100 transfected neurons from at least 3
211 independent experiments were traced. Non-paired parametric T-tests were performed in
212 Prism6 (Graphpad software, RRID:SCR_002798) to statistically analyze the data.

213

214 *miRNA target finding and validation*

215 The MiRecords database was used to search for shared mRNA targets of miR-135a and miR-
216 135b, predicted by at least 6 target prediction programs (Xiao et al., 2009).

217 Predicted targets shared by miR-135a and miR-135b were post-selected on basis of
218 potential involvement in neuronal development. For target validation, the entire 3'-UTR from
219 *KLF4* was retrieved from cDNA and cloned into the psiCHECK2 vector (Promega). PCR-
220 mediated mutagenesis of the *KLF4* 3'-UTR was performed to alter the binding site located at
221 394 nt of the *KLF4* 3'-UTR (Figure 5A, arrow). HEK293 cells (RRID:CVCL_0045) were
222 transfected using Lipofectamine with 250 ng vector and 20 pmol miRIDIAN miRNA mimic
223 (Dharmacon). Cells were lysed 24 h post-transfection and examined with Dual-Luciferase
224 reporter assay (E1960, Promega) on a spectrophotometer. T-tests were performed to compare
225 luciferase activity in Prism6 (Graphpad Software, RRID:SCR_002798).

226 For protein analysis, miRIDIAN miRNA mimics (Dharmacon) were transfected into
227 Neuro2A cells (ATCC, RRID:CVCL_0470) using Lipofectamine 2000. After 24 h, cells were

228 lysed in lysis buffer (20 mM Tris pH 8.0, 150 mM KCL, 1% Triton-X-100, protease inhibitor
229 (Roche) in MQ). Samples were separated on 8% SDS-page gels and blotted onto
230 nitrocellulose membrane. Non-specific binding was blocked with 5% milk in TBS-tween for
231 1h at RT. After incubation with rabbit-anti-KLF4 (1:500, Santa-Cruz, RRID:AB_669567) and
232 mouse-anti- β -actin (1:5000, Sigma, RRID:AB_476743) in 1% milk in TBS-tween, blots were
233 stained with peroxidase-conjugated secondary antibodies (Abcam). Signals were detected
234 using Pierce ECL Western Detection Reagent (Thermo Scientific), and images were made
235 using FluorChem M Imaging system (Protein Simple). ImageJ was used to determine protein
236 levels in the individual bands, and KLF4 expression was normalized to β -actin levels in the
237 same sample. T-tests were performed to compare the relative KLF4 expression between
238 conditions (Graphpad Prism6 software, RRID:SCR_002798).

239

240 *Immunohistochemistry*

241 E16.5 C57BL/6J mouse embryos or adult mice were collected and decapitated. Brains were
242 fixed in 4% PFA in PBS and cryoprotected in 30% sucrose in PBS. Twenty μ m thick coronal
243 brain cryosections were made. Sections were incubated with rabbit anti-KLF4 (Santa-Cruz,
244 1:500 (no longer available) or LabNed LN2023880 1:100, RRID:AB_2687557) diluted in 3%
245 BSA and 0.1% Triton-X-100 in PBS, stained with Alexa Fluor-conjugated secondary
246 antibody and counterstained with DAPI. Images were made using an AxioScope EPI-
247 fluorescent microscope (Zeiss) and a confocal scanning microscope (Olympus).

248

249 *Ex vivo electroporation*

250 Ex vivo electroporation was performed as described previously (Yau et al., 2014). In brief,
251 pregnant C57Bl/6 mice were sacrificed by cervical dislocation and E14.5 embryos were
252 rapidly removed and decapitated. 30 μ M miRIDIAN mimics (Dharmacon) for miR-135a,

253 miR-135b or control-1 combined with 0.4 $\mu\text{g}/\mu\text{l}$ pCAG-GFP vector were dissolved in 0,1%
254 Fast Green in MQ, and 1.7 μl of this mixture was injected in the lateral ventricles using glass
255 micro-pipettes (Harvard Apparatus) and a microinjector. Heads were subjected to three 100
256 ms pulses of 30 V with 100 ms pulse interval, using gold plated gene paddle electrodes and an
257 830 square wave generator (BTX Harvard Apparatus). Brains were then isolated, collected in
258 cHBSS, embedded in 3% LMP-Agarose (Fisher Scientific) in cHBSS and sectioned coronally
259 into 250 μm thick slices using a vibratome (Leica). Sections were collected on poly-D-lysine-
260 laminin-coated culture membrane inserts (Falcon), placed on top of slice culture medium
261 (70% v/v Basal Eagle Medium, 26% v/v cHBSS, 20 mM D-glucose, 1 mM L-glutamine,
262 penicillin/streptomycin) and cultured for 4 days to assess the degree of migration. Cultures
263 were fixed with 4% PFA, blocked in 3% BSA and 0.1% triton in PBS, and stained with rabbit
264 anti-GFP (1:1000, A-11122, Invitrogen, RRID:AB_221569) and mouse anti-MAP2 SMI 52
265 (1:1000, Abcam, RRID:AB_776173) antibodies. Z-stack images were taken using confocal
266 laser-scanning microscopy (Olympus). Migration of GFP-positive cells was analyzed as
267 follows: using Adobe Photoshop, consistent rectangles divided in 8 equal bins were placed on
268 top of the image, so that bin 1 includes the ventricular zone (vz) and bin 8 covers the marginal
269 zone (mz, as shown schematically in Figure 4A). Cells in each bin were counted and divided
270 by the total amount of cells in the rectangle. The average of at least two rectangles of each
271 image was used for comparison. For each condition, 12 cortical slices from at least 3 different
272 experiments were used. Non-parametric Mann-Whitney U tests were performed in Prism6
273 (Graphpad software, RRID:SCR_002798) to compare migration between control and miRNA
274 overexpression.

275

276 *In utero electroporation*

277 *In utero* electroporation was performed as described previously (van Erp et al., 2015).
278 Pregnant C57Bl/6 mice at E14.5 were deeply anaesthetized with Isoflurane (induction: 3-4%,
279 surgery: 1.5-2%), injected with 0.05 mg/kg buprenorfinhydrochloride in saline, and hereafter
280 the abdominal cavity was opened under sterile surgical conditions. Uterine horns were
281 exposed and 1.7 μ l DNA mixture containing 0.4 μ g/ μ l pCAG-GFP, and 15 μ M miR-135a and
282 15 μ M miR-135b mimic, or 30 pmol control-1 mimic, or 0.6 μ g/ μ l scrambled sponge vector,
283 or 0.3 μ g/ μ l miR-135a sponge vector and 0.3 μ g/ μ l miR-135b sponge vector (H1-mCherry
284 vectors, Tebu-bio) dissolved in MQ with 0.05% Fast Green (Sigma) was injected in the lateral
285 ventricles of the embryo's using glass micro-pipettes (Harvard Apparatus) and a PLI-100
286 Pico-injector (Harvard Apparatus). For rescue experiments, 0.2 μ g/ μ l pCAG-GFP was
287 combined with 0.2 μ g/ μ l pCAG-KLF4, and 15 μ M miR-135a and 15 μ M miR-135b mimic.
288 Brains were electroporated using an ECM 830 Electro-Square-Porator (Harvard Apparatus)
289 set to five unipolar pulses at 30 V (50 ms pulse length interval and 950 ms pulse length). The
290 motor cortex was targeted by holding the head with a platinum tweezer-electrode (negative
291 pole) while a third a gold-plated Genepaddle (positive pole, Fisher Scientific) was placed on
292 top of the head. Embryos were placed back into the abdomen, and abdominal muscles and
293 skin were sutured separately. Release from isoflurane awakened the mother mice. Embryos
294 were collected at E16.5 and pups at P4 or P10. Heads were fixed in 4% PFA in PBS and
295 submerged in 30% sucrose. 20 μ m thick coronal cryosections were made and
296 immunohistochemistry and cortical migration analysis were performed as described for *ex*
297 *vivo* electroporated slices. To measure neurite outgrowth *in vivo*, leading process length was
298 traced using ImageJ. In the case of endogenous miR-135 down-regulation, where brains were
299 electroporated with H1-mCherry sponge vectors (Tebu-bio), neuron migration and leading
300 process length were analyzed upon staining with rabbit-anti-RFP (1:1000, Rockland,
301 RRID:AB_11182807). Control and miRNA test conditions were always equally distributed

302 among the embryos in the uterus. Analysis was always performed on the slice in which the
303 corpus callosum was first complete and in 1 or 2 consecutive slices. At least 5 embryos from
304 at least 2 separate experiments were used for comparison.

305

306 *Optic nerve injury and in vivo gene transfection*

307 3-week-old C57BL/6J mice were obtained from SLC company (Hamamatsu, Japan). Optic
308 nerve injury was performed as previously described in detail (van Erp et al., 2015). The left
309 optic nerve was crushed with fine forceps for 10 sec approximately 1 mm posterior to the
310 optic disc. 50 pmol/ μ l miR-135a and 50 pmol/ μ l miR-135b or 100 pmol/ μ l control-1 mimic
311 were injected intravitreally (with lipofectamine) immediately following injury and on day 7
312 post-axotomy. *In vivo* gene transfection was performed as described previously (van Erp et
313 al., 2015). Briefly, pCAG-GFP or pCAG-KLF4 was mixed with miRNA mimics and
314 Lipofectamine 2000. 2 μ l of the complexes were injected intravitreally immediately following
315 injury and on day 7 post-axotomy. Nine mice were used for each group. Similarly, 4 μ g of
316 sponge vectors specifically targeting miR-135a and miR-135b or control sponge (Tebu-bio)
317 were injected intravitreally (with lipofectamine). Six mice per group were used. AAV2 virus
318 (AAV-miR-GFP-Blank Control virus, Cat.No: Am00102, GFP mmu-miR-135a-5p AAV
319 miRNA Virus, Cat.No: Amm1006802, GFP mmu-miR-135b-5p AAV miRNA Virus, Cat.No:
320 Amm1007002, abm) was injected at 7 days before optic nerve crush injury. To visualize RGC
321 axons, 1 μ l of cholera toxin β subunits conjugated to Alexa Fluor 555 (2 μ g/ μ L, Invitrogen)
322 was injected into the vitreous with a glass needle 12 days after the injury. On day 14 post-
323 axotomy, animals were perfused with 4% PFA. The eye cups with the nerve segment attached
324 were post-fixed, and immersed in 30% sucrose overnight at 4°C. Tissues were embedded in
325 Tissue Tek and serial cross-sections (16 μ m) were prepared using cryostat and collected on
326 MAS-coated glass slides (Matsunami, Osaka, Japan). Axonal regeneration was quantified by

327 counting the number of CTB-labeled fibers extending 0.2, 0.5, and 1.0 mm from the distal
328 end of the lesion site in 5 sections. The cross-sectional width of the optic nerve was measured
329 at the point at which the counts were taken and was used to calculate the number of axons per
330 millimeter of nerve width. The number of axons per millimeter was then averaged over the 5
331 sections. $\sum ad$, the total number of axons extending distance d in a nerve having a radius of r ,
332 was estimated by summing all the sections having a thickness t ($16 \mu\text{m}$): $\sum ad = \pi r^2 \times [\text{average}$
333 $\text{axons / mm}] / t$. Statistical analyses were performed using one-way ANOVAs. $p < 0.05$ was
334 considered significant.

335

336 *Experimental design and statistical analysis*

337 In this study, female and male C57Bl/6J mice were used regardless of their sex. For statistical
338 analyses, Prism 6 software (Graphpad) was used. Generally unpaired T-tests were used to
339 compare the means of two groups, with the exception of neuron migration analyses (non-
340 parametric Mann-Whitney U tests) and q-PCR analyses (single factor ANOVA). For all
341 statistical tests, significance was set at $p < 0.05$. Exact p values, t-values and degrees of
342 freedom are provided in the results, and Ns are provided in the figure legends.

343 At the start of this study an automated morphological cellomics screen of retinoic
344 acid-treated SH-SY5Y cells that were transduced with a lentiviral library containing 1140
345 unique human miRNAs (Poell et al, 2011) was performed to identify miRNAs that
346 (positively) influence neuronal features (Fig. 1A). The screen was conducted *in triplo*, and
347 morphological parameters were scored with a neuroprofiling algorithm (Table 1). To confirm
348 the effect of the most robust miRNAs, the cellomics analysis was repeated on SH-SY5Y cells
349 that were electroporated with miRNA mimics for a selection of hits. This experiment was
350 performed three times *in quadruplo* (i.e., three times four coverslips, Fig. 1E), and statistically
351 analyzed using Student T-tests.

352 Expression of miR-135a and miR-135b in the mouse brain at different ages was tested
353 by LNA *in situ* hybridization and q-PCR experiments (in tissue of at least 3 different mice per
354 age (Fig. 2)). Expression of miR-135a and miR-135b was also determined in cultured primary
355 hippocampal neurons (Fig. 3A). Q-PCR experiments were statistically analyzed using single
356 factor ANOVAs.

357 Next, the effect of miR-135a and miR-135b overexpression and down-regulation was
358 examined in primary neuron cultures. Lipofectamine-based transfections were replicated at
359 least 3 times *in triplo* (i.e., 3 times 3 coverslips). miRNA mimics were co-transfected with
360 GFP vector and in case of sponge-vectors internal RFP was exploited to trace neurite length
361 using the NeuronJ plugin of ImageJ (Fig. 3B-F). Student T-tests were performed to compare
362 the means of each group with the control condition.

363 To assess the endogenous effects of miR-135a and miR-135b during neuronal
364 development, *ex vivo* electroporation of miRNA mimics combined with a GFP vector and
365 subsequent organotypic slice cultures of mouse embryonic cortex were performed (E14, Fig.
366 4A). Embryos of one mother were divided among the three conditions to compare littermates,
367 and the experiment was repeated three times. Similar cortical slices of at least 6 embryos from
368 3 different mothers were used for comparison. Next, *in utero* electroporation experiments
369 were performed in E14 mice embryos to over-express and down-regulate miR-135a and miR-
370 135b *in vivo*. For embryonic analysis, the three conditions were divided over the embryos that
371 were present in the uterus to always compare littermates. *In utero* electroporation dedicated to
372 the isolation of postnatal tissue was performed one condition per mother. For analysis of
373 migration and neurite outgrowth of electroporated cortical neurons three consecutive
374 cryosections showing the corpus callosum were used and taken from at least 9 pups derived
375 from at least 3 different mothers. For both *ex vivo* and *in utero* electroporation analyses we
376 performed Mann-Whitney U-tests to compare the distribution of the migrating cells. These

377 were manually counted in 2-3 rasters containing 8 cortical ‘bins’ per slice placed exactly
378 perpendicular to the direction of migration, with the bottom of bin 1 touching the border of
379 the ventricle (for embryonic brains) or the axons of the anterior commissure (for postnatal
380 brains) and the top of bin 8 reaching the cortical surface (Fig. 4A).

381 Next, possible mRNA targets of miR-135a and miR-135b were identified using the
382 bio-informatic tool miRecords (Xiao et al 2009). KLF4 was selected based on its reported
383 effects on neurite outgrowth and neuronal migration. The strongest predicted binding site of
384 miR-135a and miR-135b in the KLF4 3’-UTR was selected and used for a luciferase assay
385 performed three times in HEK293 cells to confirm direct target binding (Fig. 5A, B).
386 Immunohistochemistry was then used to assess whether KLF4 and miR-135a and b are
387 expressed in similar brain areas (Fig. 5C). Next, we tested whether endogenous KLF4
388 expression in N2A cells was down-regulated upon miR-135a and miR-135b administration.
389 To determine an endogenous role for miR-135-KLF4 signaling, rescue experiments were
390 performed in primary hippocampal neuron cultures and *in utero* electroporation using KLF4
391 cDNA (insensitive to miRNA regulation) using the same experimental procedures and
392 repetitions as described before.

393 Since KLF4 is one of the most important signals counteracting axon regeneration, we
394 investigated whether miR-135a and miR-135b could be used to decrease KLF4 expression in
395 poorly regenerating neurons in a specific and cell-autonomous fashion. We first injected
396 miRNA mimics intra-vitreally (on day 0 and day 7) to learn whether this was sufficient to
397 deliver miRNAs to the optic nerve and down-regulate KLF4 expression. Q-PCR was
398 performed on 3 optic nerves per condition, 14 days after the first injection of mimics. Then,
399 mimics were combined with GFP vector and/or KLF4 cDNA to determine axon regeneration
400 14 days after optic nerve injury. This was repeated in 9 mice per condition. Q-PCR
401 experiments revealed no differences in transfection efficiency between conditions. AAV2

402 virus containing miR-135a, miR-135b, or control miRNA was injected to transduce RGCs
403 only in 6 mice 7 days before the optic nerve crush and to assess the cell-autonomous nature of
404 the effect observed with mimic injections. Finally, we determined whether miR-135a and
405 miR-135b had an endogenous role in optic nerve regeneration measured 14 days after the
406 optic nerve crush by injecting sponge vectors at day 0 and day 7 in 6 mice. Axon regeneration
407 was statistically tested by ANOVAs followed by Sidak post-hoc tests.
408

409 **Results**

410

411 *miRNome-wide screen for miRNAs that regulate neurite growth*

412 To identify miRNAs that can promote neurite growth, an image-based miRNA screen was
413 performed in neuronal SH-SY5Y cells, a cell line regularly used for cellular screening.
414 Neuronal differentiation of SH-SY5Y cells was induced by retinoic acid treatment followed
415 by transduction of a lentiviral library containing 1140 unique human miRNAs (Poell et al.,
416 2011)(Fig. 1A, B). Using a Cellomics ArrayScan platform, thousands of cells in each
417 condition were analyzed for parameters related to neuronal morphology. This multiparametric
418 analysis resulted in a cumulative hitscore that was based on parameters such as neurite length
419 and branching (Table 1). To identify hits, scores for each individual miRNA were compared
420 to the median score of all miRNAs. This approach assumes that the majority of miRNAs do
421 not affect neuronal morphology. This approach identified 13 annotated miRNAs with
422 pronounced effects on specific morphological properties of differentiated SH-SY5Y cells (e.g.
423 neurite length). Of these miRNAs, miR-135b had the largest effect (Fig. 1C).

424 To confirm the effect of miR-135b, retinoic acid-treated SH-SY5Y cells were
425 electroporated with miR-135b mimics to simulate over-expression. miR-135a, a close
426 homolog of miR-135b (Fig. 1D), was also included since it shares many mRNA targets with
427 miR-135b and because we suspected that miR-135a was not identified in the initial screen
428 because of technical problems (edge-well effects in the culture plates). miR-124, a well-
429 known brain-enriched miRNA that was identified in the screen, was also included (Fig. 1C),
430 as well as two control miRNA mimics (both originating from *C. elegans* and proven to not
431 target specific mammalian mRNAs (Dharmacon, own observations)). In line with the results
432 of the screen, miR-135b mimics affected the general morphology of SH-SY5Y cells ($6.58 \pm$
433 1.11 vs. 1.24 ± 0.50 , $t(188) = 4.64$, $p < 0.0001$ (control-1), or vs. 1.67 ± 0.52 , $t(188) = 4.19$, p

434 < 0.0001 (control-2), one-way ANOVA, Sidak post-hoc test; Fig. 1E, left panel).
435 Furthermore, miR-135b enhanced neurite outgrowth (3.53 ± 0.69 , $t(189) = 4.46$, $p < 0.0001$
436 vs. 0.55 ± 0.28 (control-1), or vs. 0.90 ± 0.35 $t(189) = 3.87$, $p = 0.0006$ (control-2), one-way
437 ANOVAs, Sidak post-hoc tests; Fig. 1E, middle panel). Total hitscore and hitscore related to
438 neurite length appeared to be affected by miR-135a, but these effects did not reach statistical
439 significance. Neurite branching was significantly increased by miR-135a (2.00 ± 0.71 , $t(189)$
440 $= 3.62$, $p = 0.0015$ vs. control-1 and $t(189) = 3.54$; $p = 0.0020$ vs. control-2) and miR-135b
441 (1.53 ± 0.36 , $t(189) = 3.11$, $p = 0.0085$ vs. control-1 and $t(189) = 3.03$, $p = 0.011$ vs. control-
442 2, one-way ANOVAs, Sidak post-hoc tests) mimics compared to control mimics (0.14 ± 0.12
443 (control-1), or 0.15 ± 0.11 (control-2); Fig. 1E, right panel). Together, these data confirm that
444 miR-135b and miR-135a increase neurite growth and complexity.

445

446 *Expression of miR-135a and miR-135b in the developing mouse cortex and hippocampus*

447 miR-135a and miR-135b sequences are preserved across species and detected in mouse brain
448 tissue (Lagos-Quintana et al., 2002; Sempere et al., 2004; Ziats and Rennert, 2014; Caronia-
449 Brown et al., 2016). However, the precise spatiotemporal pattern of expression and functional
450 role of these miRNAs in neurons remained poorly understood. Therefore, we first analyzed
451 the expression of miR-135a and miR-135b by quantitative PCR (qPCR) in the developing (at
452 E14, E16, P0 and P10 during which neurite growth and branching occur) and in adult mouse
453 cortex and hippocampus. qPCR analysis detected miR-135a and miR-135b in embryonic,
454 postnatal and adult cortex and hippocampus. Expression of both miRNAs declined as cortical
455 development progressed, but was increased again at adult stages. In contrast, while
456 hippocampal miR-135a expression decreased towards P10 and displayed higher levels again
457 at adult stages, miR-135b levels remained unchanged (Fig. 2A, C). Locked nucleic acid
458 (LNA)-based *in situ* hybridization was used to reveal the spatial distribution of both miRNAs

459 and revealed miR-135a and miR-135b expression in the cortex (at E14, P10 and adult, Fig.
460 2B) and hippocampus (at E14, P0, P10 and adult, Fig. 2D). Specific signals were observed in
461 the dentate gyrus (DG) and CA3 pyramidal cell layers of the hippocampus and in the cortical
462 plate of the developing cortex. Furthermore, both miRNAs were expressed in the adult mouse
463 brain (Fig. 2B, D). Thus, miR-135a and miR-135b display specific spatiotemporal patterns of
464 expression in the developing mouse brain.

465

466 *miR-135a and miR-135b control axon growth and branching*

467 miR-135a and miR-135b displayed prominent hippocampal expression and therefore, to
468 investigate their functional role in neurons, hippocampal neurons were dissociated,
469 transfected with miRNA mimics, and analyzed for axon growth at 4 days *in vitro* (DIV). First,
470 qPCR was used to confirm endogenous expression of miR-135a and miR-135b in primary
471 hippocampal cultures (Fig. 3A). At DIV4, the longest neurite, confirmed to be the axon, was
472 significantly longer in neurons transfected with miR-135a ($354.9 \pm 24.41 \mu\text{m}$) or miR-135b
473 ($392.8 \pm 15.24 \mu\text{m}$) mimics as compared to control ($271.7 \pm 7.18 \mu\text{m}$, $t(776) = 4.443$
474 (Control-1 vs. miR-135a), $t(900) = 8.181$ (Control-1 vs. miR-135b), both $p < 0.0001$,
475 unpaired T-tests; Fig. 3B and C). Co-transfection of both miR-135a and miR-135b further
476 increased axon length ($428.7 \pm 14.97 \mu\text{m}$, vs. Control-1 $t(1022) = 10.36$, $p < 0.0001$; vs. miR-
477 135a $t(590) = 2.628$, $p = 0.0088$, unpaired T-tests). To assess the endogenous roles of miR-
478 135a and miR-135b specific miRNA sponges designed to sequester miR-135a and miR-135b
479 were co-transfected into hippocampal neurons. Decreased availability of the miRNAs resulted
480 in a significant decrease in axon length ($270.1 \pm 13.63 \mu\text{m}$) compared to scrambled control
481 sponge transfection ($340.1 \pm 18.09 \mu\text{m}$, $t(211) = 3.053$, $p = 0.0026$, unpaired T-test; Fig. 3E).
482 Since the initial screen in SH-SY5Y cells showed effects on both neurite growth and
483 branching, Sholl analysis was performed on primary hippocampal neurons transfected with

484 miR-135a, miR-135b and the combination of the two mimics. Over-expression of both
485 miRNAs alone and combined resulted in a marked increase in neurite branching in more
486 distal regions (Fig. 3F). Interestingly, combined over-expression of miR-135a and miR-135b
487 or of miR-135b alone also resulted in increased branching in the area close to the cell body.
488 These data suggest an increase in the number of (branches of-) primary neurites (blue
489 neurites) and increased branching of the axon (red neurites) (control-1 vs. miR-135a: t(12800)
490 ranges from 3.728 to 8.52, control-1 vs. miR-135b: t(13144) ranges from 3.735 to 6.426;
491 control-1 vs. miR-135ab: t(12164) ranges from 3.84 to 7.496; $p < 0.001$ for all; unpaired T-
492 tests). The number of cumulative intersections of neurites with the Sholl circles was also
493 higher in miR-135ab treated neurons (53.9 ± 4.91) as compared to control (38.69 ± 2.67 , t(37)
494 = 2.414, $p = 0.021$, unpaired T-test; Fig. 3G). Together, these experiments show that miR-
495 135a and miR-135b regulate axon growth and branching.

496

497 *Cortical neuron migration requires miR-135a and miR-135b*

498 miR-135a and miR-135b are expressed in hippocampal and cortical neurons as they migrate
499 in the developing nervous system and extend neurites (Fig. 2) and manipulation of these
500 miRNAs affects neuronal morphology in cultured hippocampal but also cortical neurons (Fig.
501 3; data not shown). To next assess the role of miR-135a and miR-135b in neurons in the
502 complex environment of the embryonic brain, we performed *ex vivo* and *in utero*
503 electroporation (van Erp et al., 2015). *Ex vivo* electroporation of mouse cortex with miR-135a
504 and miR-135b mimics was performed at E14.5, brains were sliced and cultured, and analyzed
505 at DIV4. Electroporation of miR-135a or miR-135b mimics induced a marked increase in the
506 migration of cortical neurons from the ventricular zone (VZ) to the cortical plate (CP),
507 exemplified by a larger number of electroporated GFP-positive neurons in the CP and fewer
508 cells in the intermediate zone (IZ), as compared to control mimic conditions (Fig. 4A, see

509 figure legend for statistical results). To confirm these effects *in vivo*, we delivered miRNA
510 mimics or sponges to the E14.5 cortex by *in utero* electroporation and analyzed migrating
511 neurons at E16.5. Mimics for miR-135a and miR-135b were combined to elicit significant
512 phenotypes in a short time period. In line with the *ex vivo* electroporation data, delivery of
513 miR-135ab mimics to the cortex enhanced neuronal migration towards the pial surface and
514 induced a concomitant depletion in deeper layers such as the SVZ (Fig. 4B, see figure legend
515 for statistical results). Electroporation of miR-135a and miR-135b sponges had a small, but
516 opposite effect, i.e. delayed migration of cortical neurons, confirming an endogenous
517 requirement for miR-135a and miR-135b in cortical neuron migration (Fig. 4C, see figure
518 legend for statistical results). As a measure for *in vivo* neurite outgrowth, we quantified the
519 length of the leading process of migrating neurons following *in utero* electroporation. While
520 miR-135a and miR-135b mimics induced an increase in leading process length (30.65 ± 1.09
521 vs. 23.91 ± 1.01 , $t(364) = 4.497$, $p < 0.0001$, unpaired T-test; Fig. 4B), leading processes were
522 shorter after application of miR-135 sponges (25.23 ± 0.80 vs. 33.78 ± 1.28 , $t(325) = 5.712$, p
523 < 0.0001 , unpaired T-test; Fig. 4C). To assess the long-term effect of miR-135 over-
524 expression *in vivo*, we isolated the brains from embryos *in utero* electroporated at E14.5 at P4
525 (Fig. 4D) and P10 (Fig. 4E). Interestingly, at P4 electroporation of miR-135a and miR-135b
526 significantly enhanced neuron migration resulting in a larger number of neurons in upper
527 cortical areas (Fig. 4D, see figure legend for statistical results). At P10, a small but significant
528 difference in the distribution of cells in the upper cortical layers remained between embryos
529 electroporated with control or miR135 mimics (Fig. 4E, see figure legend for statistical
530 results). Overall, these data suggest that, in line with their effects in cultured neurons, miR-
531 135a and miR-135b control neurite length and neuron migration *in vivo*.

532

533 *miR-135a and miR-135b control axon growth and neuronal migration through KLF4*

534 How do miR-135a and miR-135b control neuronal morphology and migration? Based on high
535 sequence similarity and comparable biological effects in neurons, we hypothesized that
536 miRNA-135a and miRNA-135b may share many of their mRNA targets. To identify those
537 targets, we performed target prediction analysis using miRecords (Xiao et al., 2009). By
538 combining data from at least 6 databases in miRecords, 57 overlapping targets were found for
539 miR-135a and miR-135b (Table 2). Several of these targets had confirmed roles in neurite
540 growth and neuronal morphology. However, for many of these targets (e.g. PTK2, TAF4)
541 knockdown had been reported to reduce neurite growth or neuron migration (data not shown).
542 KLF4 was particularly interesting as knockdown of KLF4 in neurons, similar to
543 overexpression of miR-135s, enhances axon growth, leading process length and neuronal
544 migration (Moore et al., 2009; Qin and Zhang, 2012). Furthermore, recent work in vascular
545 smooth muscle and hepatocellular carcinoma cells links miRNA-135a to KLF4 (Lin et al.,
546 2016; Yao et al., 2016). Finally, KLF4 contains predicted binding sites for several miRNAs in
547 the top list of our initial screen (miR-124, miR-449, miR-488, miR-499; Fig. 1C). The 3'-
548 UTR of KLF4 harbours two predicted miR-135 binding sites (Fig. 5A) and to confirm that
549 KLF4 is a bona fide target for miR-135s we first performed dual-luciferase reporter assays by
550 co-transfecting psiCHECK2-KLF4 3'-UTR and miR-135a and miR-135b mimics into
551 HEK293 cells. miR-135a and miR-135b mimics significantly decreased luciferase activity
552 both when transfected alone or when combined (Fig. 5B). To confirm direct and specific
553 binding, the miRNA-135 binding site that was predicted to have the strongest association
554 (according to www.microRNA.org) was mutated (site 394; Fig. 5A). This mutation
555 completely abolished miR-135-mediated effects on luciferase activity, suggesting that site
556 394 is the main miR-135 binding site in KLF4 (KLF4 WT miR-135a vs. KLF4 mutated miR-
557 135a, $t(4) = 4.715$, $p = 0.0092$; KLF4 WT miR-135b vs. KLF4 mutated miR-135b, $t(4) =$
558 2.933 , $p = 0.0427$; KLF4 WT miR-135ab vs. KLF4 mutated miR-135ab, $t(4) = 4.735$, $p =$

559 0.0091, Unpaired T-test) (Fig. 5B). Next, we performed immunohistochemistry for KLF4 to
560 assess whether miR-135s and KLF4 are expressed in the same brain regions. Indeed, in line
561 with our *in situ* hybridization data for miR-135a and miR-135b, prominent KLF4 expression
562 was detected in neurons in the CP of the E16.5 and adult cortex and in the developing and
563 adult hippocampus (Fig. 5C). To further validate the relation between miR-135 and KLF4,
564 endogenous KLF4 protein levels were analyzed in transfected Neuro2A cells by Western blot.
565 Reduced KLF4 expression was observed after transfection with miR-135a and miR-135b
566 mimics as compared to control mimic transfection (miR-135ab vs. Control-1: 0.378 ± 0.032
567 vs. 0.643 ± 0.01 , $t(10) = 3.170$, $p = 0.010$, Unpaired T-test; Fig. 5D). Together, these data
568 indicate that KLF4 is a target for miR-135a and miR-135b.

569 Next, we assessed whether the effects of miR-135s (miR-135a and miR-135b) on axon
570 growth and neuronal migration require KLF4. In primary hippocampal neurons, co-
571 transfection of KLF4 cDNA lacking the 3'-UTR (KLF4 Δ 3'-UTR), and therefore miR-135
572 binding sites, markedly reduced the increase in axon growth by transfection of miR-135
573 mimics (Fig. 5E, Control-1 vs. Control-1+KLF4: 271.1 ± 7.178 vs. $239.9 + 9.701$, $t(785) =$
574 2.250 , $p = 0.025$; Control-1 vs. miR-135ab+KLF4: 271.1 ± 7.178 vs. 331.7 ± 10.92 , $t(980) =$
575 4.787 , $p < 0.0001$; miR-135ab+KLF4 vs. miR-135ab: 331.7 ± 10.92 vs. 428.7 ± 14.97 , $t(794)$
576 $= 5.139$, $p < 0.0001$, Unpaired T-test). Fig. 5F). Similarly, the positive effect of miR-135a and
577 miR-135b over-expression on cortical neuron migration and leading process length was
578 normalized by co-electroporation of KLF4 Δ 3'-UTR (see figure legend for statistical results of
579 neuronal migration, for leading process length: miR-135ab: 32.34 ± 1.084 , miR-
580 135ab+KLF4: 20.42 ± 0.79 , $t(240) = 8.851$, $p < 0.0001$. Unpaired T-test. Fig. 5G). Together,
581 these experiments indicate that miRNA-135s enhance axon growth and neuronal migration by
582 repressing KLF4 protein expression.

583

584 *Exogenous miR-135 application promotes optic nerve regeneration through KLF4*
585 Lowering neuronal KLF4 expression not only promotes axon growth in developing neurons
586 but is also one of the few experimental treatments that facilitates regenerative axon growth
587 following CNS injury. Knockout mice lacking KLF4 showed significantly enhanced retinal
588 ganglion cell (RGC) axon regeneration following optic nerve injury (Moore et al., 2009; Qin
589 et al., 2013) This effect of KLF4 requires downstream signalling via the Janus kinase (JAK)-
590 signal transducer and activator of transcription 3 (STAT3) pathway (Qin et al., 2013), but
591 upstream regulatory mechanisms of this pathway remain unknown. Because of these results
592 and our data showing that miR-135 mimics can promote axon growth by reducing KLF4
593 expression, we next asked whether application of miR-135 mimics can facilitate regenerative
594 axon growth in the CNS. To test this hypothesis, we used the optic nerve crush model.
595 siRNAs and miRNA mimics can be efficiently targeted to adult RGCs and optic nerve
596 regeneration can be reliably quantified (Dickendesher et al., 2012; van Erp et al., 2015).
597 Further, both KLF4 and miR-135s are expressed in adult mouse RGCs and reducing KLF4
598 expression enhances optic nerve regeneration (Moore et al., 2009; Qin et al., 2013). First, we
599 confirmed that intravitreal injection of miR-135 mimics leads to an elevation of miR-135a
600 and miR-135b levels (Fig. 6A, B). Although endogenous expression of miR-135s was
601 detected, intravitreal injection of mimics markedly increased miR-135a and miR-135b
602 expression, as compared to injections with scrambled controls (Ctrl1 vs. miR-135a: $t(4) =$
603 $2.462, p = 0.0348$; Ctrl1 vs. miR-135b: $t(4) = 4.309, p = 0.0063$, Unpaired T-test). In line with
604 our data identifying KLF4 as a miR-135 target (Fig. 5), injection of miR-135 mimics in the
605 eye led to a decrease in KLF4 expression (Ctrl1 vs. miR-135ab: $t(3) = 2.901, p = 0.0312$,
606 Unpaired T-test. Fig. 6C). Next we assessed the effect of miR-135 injection on optic nerve
607 regeneration. Following administration of scrambled control mimics, most CTB-labeled RGC
608 axons stopped abruptly at the crush site and only few fibers crossed the lesion into the distal

609 nerve (Fig. 6D, E). In contrast, miR-135 mimics induced significant regeneration (0.2 mm,
610 Control-1+GFP vs. miR-135ab+GFP: 46.89 ± 6.816 vs. 208.4 ± 35.11 , $t(96) = 7.374$, $p <$
611 0.0001 . one-way ANOVA with Sidak post-hoc test) beyond the lesion site and more
612 pronounced sprouting in the distal segment of the nerve (Fig. 6D, E). To examine whether
613 this effect was caused by the ability of miR-135s to reduce KLF4 expression, we combined
614 intravitreal injection of miR-135 mimics with co-transfection of vectors expressing GFP
615 (pCAG-GFP) or a KLF4 cDNA which is not targeted by miR-135s (pCAG-KLF4) (van Erp et
616 al., 2015). Overexpression of KLF4 did not affect RGC axon regeneration, but partly
617 normalized the regeneration promoting effect of miR-135 mimic injection following ONI (0.2
618 mm, Control-1+GFP vs. miR-135ab+KLF4: 46.89 ± 6.816 vs. 115.4 ± 24.63 , $t(96) = 3.128$, p
619 $= 0.028$, one-way ANOVA with Sidak post-hoc test) (Fig. 6D, E). Importantly, this effect of
620 KLF4 was not due to its ability to regulate miR-135 expression as miR-135a and miR-135b
621 levels in the retina were similar following miR-135ab + GFP and miR-135ab + KLF4
622 administration (Fig. 6F).

623 Intravitreal injection may target miRNA mimics to different cell types in the mouse
624 retina. To ensure that miR-135a and miR-135b can have a positive, cell autonomous effect in
625 RGCs on axon regeneration, overexpression of both miRNAs was induced by intravitreal
626 injection of AAV2, a viral serotype known to specifically target RGCs (Fig. 6A, G)(Weitz et
627 al., 2013). Indeed, targeting miR-135s to RGCs induced RGC axon regeneration at a level
628 comparable to that observed following mimic injection (0.2 mm, AAV2-Control vs. AAV2-
629 miR-135ab: 53.76 ± 10.62 vs. 243.6 ± 23.59 , $t(30) = 10.98$, $p < 0.0001$. one-way ANOVA
630 with Sidak post-hoc test) (Fig. 6H). Finally, to assess a potential endogenous role of miR-
631 135a and miR-135b in regenerating RGC axons specific miRNA sponges designed to
632 sequester miR-135a and miR-135b were injected intravitreally. Decreased availability of the
633 miRNAs resulted in a small but significant decrease in the number of regenerating axons

634 close to the injury site compared to scrambled control sponge transfection (0.2 mm, Control
635 sponge vs. miR-135a/b sponge: 49.6 ± 4.566 vs. 28.46 ± 7.593 , $t(18) = 3.589$, $p = 0.0063$. one-
636 way ANOVA with Sidak post-hoc test) (Fig. 6I). Together, these results indicate that
637 overexpression of miR-135 promotes CNS axon regeneration in part by reducing KLF4
638 expression, while decreasing functional miR-135 levels further reduces the regenerative
639 potential of adult RGCs.

640 **Discussion**

641

642 miRNAs are highly abundant in neurons and have been linked to various aspects of neuronal
643 development and function. However, the *in vivo* function(s) and downstream mRNA targets
644 of many of the neuronally expressed miRNAs remain unknown. Here, we performed high
645 content screening of more than one thousand miRNAs in neuronal cells and identified
646 miRNA-135a and miRNA-135b as potent stimulators of axon growth and neuron migration
647 through the inhibition of the transcription factor KLF4. Further, although injured CNS axons
648 generally lack significant regenerative capacity, our data show that repression of KLF4 by
649 intravitreal application of miRNA-135 mimics promotes regeneration of RGC axons
650 following optic nerve injury. In contrast, lowering miR-135 levels further inhibited RGC axon
651 regeneration. Together, these results identify novel neuronal roles for the miRNA-135-KLF4
652 pathway and show that ectopic miRNA application to injured neurons can be used to enhance
653 mammalian CNS axon regeneration.

654

655 *Novel neuronal functions for miR-135a and miR-135b*

656 The expression of members of the miR-135 family is regulated in specific types of cancer.
657 miRNA-135s target many different tumour-related genes and thereby affect cell proliferation,
658 differentiation, and metastasis formation (e.g. (Nagel et al., 2008; Lin et al., 2013; Valeri et
659 al., 2014; Ren et al., 2015; Shi et al., 2015)). Because of their important role in cancer, both
660 the diagnostic and therapeutic use of miR-135s are being intensely investigated (Khatri and
661 Subramanian, 2013; Wu et al., 2014; Zhang et al., 2016). Despite specific expression of miR-
662 135s in the developing and adult nervous system (Fig. 2) (Lagos-Quintana et al., 2001;
663 Sempere et al., 2004; Ziats and Rennert, 2014; Caronia-Brown et al., 2016), much less is
664 known about the neuronal functions of miR-135s. miR-135a is required for chronic stress

665 resiliency, antidepressant efficacy and 5-HT activity in adult mice (Issler et al., 2014), and
666 may contribute to early mouse brain development (Caronia-Brown et al., 2016). At the
667 cellular level, miR-135s mediate long-lasting spine remodelling in hippocampal synaptic LTD
668 by targeting complexin-1 and -2 (Hu et al., 2014). Previous work and our current results show
669 developmentally regulated expression patterns for both miR-135a and miR-135b during late
670 embryonic and postnatal development (Ziats and Rennert, 2014). However, the role of miR-
671 135s at these developmental stages was unknown. Interestingly, miR-135b was the top hit of
672 our image-based miRNA screen for neuronal morphology and subsequent experiments
673 confirmed and extended this observation by revealing that neuronal miR-135b and its
674 homolog miR-135a are required for neurite outgrowth and cortical neuron radial migration *in*
675 *vitro* and *in vivo*. These observations reveal novel functions for miR-135a and miR-135b and
676 are intriguing as miR-135a has been linked to disorders such as epilepsy and schizophrenia,
677 which are characterized by structural changes in neuronal networks (e.g. (Kan et al., 2012;
678 Rossi et al., 2014; Alsharafi and Xiao, 2015)). For example, expression of miR-135a is
679 upregulated in the hippocampus of patients suffering from temporal lobe epilepsy (Kan et al.,
680 2012) and it will be interesting to determine whether, and if so how, this miRNA contributes
681 to pathogenic processes such as mossy fiber sprouting and granule cell dispersion observed
682 during epilepsy.

683

684 *KLF4 is a downstream target of miR-135a and miR-135b in neurons*

685 In this study, we identified KLF4 as a target of miR-135a and miR-135b in neurons. KLF4 is
686 a transcription factor that, apart from its function in self-renewal of embryonic stem cells,
687 regulates the intrinsic neurite growth capacity of neurons (Moore et al., 2009; Steketee et al.,
688 2014). Over-expression of KLF4 in RGCs strongly represses neurite outgrowth and
689 branching. Conversely, down-regulation of KLF4 induces longer neurites and enhances

690 cortical neuron migration (Qin and Zhang, 2012; Fang et al., 2016). KLF4 is down-regulated
691 during neuronal differentiation and development, and KLF4 over-expression impairs neural
692 progenitor cell proliferation and differentiation (Qin et al., 2011). KLF4 expression gradually
693 increases in mature neurons, correlating with a gradual loss in the ability of neurons to regrow
694 their neurites (Moore et al., 2009; Blackmore et al., 2010). Several of our observations
695 identify KLF4 as an important neuronal target of miR-135s. First, miR-135 mimics
696 downregulate KLF4 expression in luciferase assays, neuronal cells and in RGCs *in vivo*. This
697 is in line with the ability of miR-135a to negatively regulate KLF4 and KLF4-dependent
698 STAT3 signalling in non-neuronal cells (Lin et al., 2016; Yao et al., 2016). Second, KLF4
699 knockdown and miR-135 overexpression have similar effects on neuron migration, neurite
700 growth, leading process length and RGC axon regeneration. Third, the neurite (re-)growth and
701 neuron migration promoting effects of miR-135 overexpression can be rescued by expression
702 of miR-135-insensitive KLF4 constructs. Interestingly, whereas overexpression of KLF4 fully
703 rescues the positive effects of miR-135s on cortical neuron migration, it only partially
704 reverses the effects of these miRNAs on neurite growth and regeneration. It is formally
705 possible that the levels of exogenous KLF4 expression were insufficient to reverse KLF4
706 expression to endogenous levels. Alternatively, as miRNAs are known to target multiple
707 different mRNAs, it is possible that miR-135 mimics affect different transcripts related to
708 neurite growth and migration other than KLF4. Indeed, in non-neuronal cells miR-135a and
709 miR-135b are known to for example target *APC*, *GSK3 β* and *FOXO1*, all of which have been
710 implicated in neurite growth or neuron migration (Nagel et al., 2008; Moritoki et al., 2014;
711 Yang et al., 2015)(data not shown). Furthermore, KLF4 is part of a larger family of KLF
712 proteins, several of which regulate axon growth (Apara and Goldberg, 2014). Bio-informatics
713 analysis reveals that other family members, including KLF6, 8, 9, 13, and 16, have predicted
714 binding sites for miR-135a and miR-135b in their 3'-UTRs (data not shown).

715

716 *Exogenous Application of miR-135s Enhances CNS Axon Regeneration*

717 The expression of miRNAs is strongly regulated following injury to the peripheral and central
718 nervous systems. Knockout of Dicer, a protein required for miRNA biogenesis, hampers
719 peripheral nerve regeneration, while select miRNAs can function as intrinsic inhibitors of
720 CNS axon regeneration (e.g. (Song et al., 2012; Wu et al., 2012; Zou et al., 2013; Hancock et
721 al., 2014; Phay et al., 2015; Li et al., 2016; Martirosyan et al., 2016)). In line with these
722 observations, manipulation of miRNA expression in mammalian adult sensory neurons
723 promotes the regeneration of their axons in the PNS and CNS (e.g. (Jiang et al., 2015; Gaudet
724 et al., 2016; Hu et al., 2016)). However, whether or not direct manipulation of miRNAs in
725 injured mammalian CNS neurons also enhances axon regeneration, and if so, through which
726 mRNA targets, was unknown.

727 KLF4 binds STAT3 and represses the JAK-STAT3 pathway (Qin et al., 2013). Optic
728 nerve crush experiments have shown that down-regulation of KLF4 and concomitant
729 activation of JAK-STAT3 signalling markedly induces regenerative axon growth in the
730 hostile CNS environment (Moore et al., 2009; Qin et al., 2013). The fact that miR-135b was
731 the top hit of our functional screen together with the ability of miR-135b and miR-135a to
732 promote axon growth through repression of KLF4 prompted us to explore whether miR-135s
733 could be used to stimulate axon regrowth following CNS injury. Intravitreal administration of
734 miR-135 mimics to the retina following optic nerve injury reduced retinal KLF4 levels and
735 triggered RGC axon regrowth into and across the lesion site. This effect of miR-135s was in
736 part KLF-dependent as re-expression of KLF4 in RGCs partially reversed the regrowth
737 phenotype. Further, targeting miR-135s specifically to RGCs by viral vector-mediated
738 delivery was sufficient to promote RGC axon regeneration. Previous studies have shown that
739 miRNAs can be used to stimulate axon regeneration in the injured CNS (e.g. (Jiang et al.,

740 2015; Gaudet et al., 2016; Hu et al., 2016)). Our findings are, however, conceptually distinct
741 from these previous reports: we find that application of miRNAs to injured CNS neurons
742 triggers axon regeneration following CNS injury, rather than regeneration of peripheral
743 sensory axons in the CNS following delivery of miRNAs to the injury site. Thus, while
744 previous work has shown that miRNAs can be used to render the injured CNS more
745 permissive for CNS axon regeneration, our work now shows that miRNAs can also be
746 employed to elevate the intrinsic growth potential of injured CNS neurons and thereby elicit
747 regenerative growth. The ability of KLF4 re-expression to only partially rescue the
748 regeneration-promoting effects of miRNA-135s supports the idea that these miRNAs target
749 several different transcripts in the injured retina. miRNA-mRNA binding only requires a ~7 –
750 8 nucleotides match between miRNA and mRNA, so an individual miRNA can have dozens
751 or possibly hundreds of targets. A single miRNA can regulate several genes in a single
752 pathway or single genes in several pathways. This multi-targeting property has obvious
753 applications for promoting axon regeneration since it offers the means to disrupt several
754 processes at once; a feature likely to be necessary for any future disease-modifying therapy.
755 Also, several different miRNAs may be combined into one therapy to target different cellular
756 processes affecting regeneration, e.g. glial scar formation and inflammation.

757 In conclusion, this study identifies miR-135a and miR-135b as novel regulators of
758 intrinsic neurite outgrowth capacity and neuron migration by targeting KLF4. In addition, we
759 find that exogenous application of miR-135 mimics to injured CNS neurons inhibits the
760 intrinsic growth inhibitor KLF4 and thereby enhances CNS axon regeneration. Vice versa,
761 reducing miR-135 levels in the retina further decreased RGC axon regeneration. These data
762 provide new tools for enhancing CNS axon regeneration and underscore the crucial role of
763 these small non-coding RNAs following neural injury. While most studies select miRNAs on
764 basis of spatiotemporal expression or downstream targets, we have used high-content

765 screening as an alternative and powerful strategy to identify novel neurite growth promoting
766 miRNAs. Our screen identified several miRNAs with potent effects on neurite growth and
767 branching. These included miRNAs with known effects on neurite development (e.g. miR-
768 124) but also previously unexplored candidates (e.g. miR-220b). Further work is needed to
769 firmly establish the function of these miRNAs and whether their aberrant expression or
770 function is functionally linked to neural disorders such as epilepsy.

771

772 **References**

773

774 Aksoy-Aksel A, Zampa F, Schrott G (2014) MicroRNAs and synaptic plasticity--a mutual
775 relationship. *Philos Trans R Soc Lond B Biol Sci* 369:20130515–20130515 Available at:
776 <http://rstb.royalsocietypublishing.org/cgi/doi/10.1098/rstb.2013.0515> [Accessed January
777 27, 2017].

778 Alsharafi W, Xiao B (2015) Dynamic Expression of MicroRNAs (183, 135a, 125b, 128, 30c
779 and 27a) in the Rat Pilocarpine Model and Temporal Lobe Epilepsy Patients. *CNS*
780 *Neurol Disord Drug Targets* 14:1096–1102 Available at:
781 <http://www.ncbi.nlm.nih.gov/pubmed/25801837> [Accessed February 1, 2017].

782 Apará A, Goldberg JL (2014) Molecular mechanisms of the suppression of axon regeneration
783 by KLF transcription factors. *Neural Regen Res* 9:1418–1421 Available at:
784 <http://www.nrroonline.org/text.asp?2014/9/15/1418/139454> [Accessed February 1, 2017].

785 Baldwin KT, Giger RJ (2015) Insights into the physiological role of CNS regeneration
786 inhibitors. *Front Mol Neurosci* 8:23 Available at:
787 <http://www.ncbi.nlm.nih.gov/pubmed/26113809> [Accessed January 27, 2017].

788 Baudet M-L, Bellon A, Holt CE (2013) Role of microRNAs in Semaphorin function and
789 neural circuit formation. *Semin Cell Dev Biol* 24:146–155 Available at:
790 <http://www.ncbi.nlm.nih.gov/pubmed/23219835> [Accessed January 31, 2017].

791 Blackmore MG, Moore DL, Smith RP, Goldberg JL, Bixby JL, Lemmon VP (2010) High
792 content screening of cortical neurons identifies novel regulators of axon growth. *Mol*
793 *Cell Neurosci* 44:43–54 Available at:
794 <http://linkinghub.elsevier.com/retrieve/pii/S1044743110000254> [Accessed February 1,
795 2017].

796 Caronia-Brown G, Anderegg A, Awatramani R (2016) Expression and functional analysis of

- 797 the Wnt/beta-catenin induced mir-135a-2 locus in embryonic forebrain development.
798 Neural Dev 11:9 Available at:
799 <http://neuraldevelopment.biomedcentral.com/articles/10.1186/s13064-016-0065-y>
800 [Accessed February 1, 2017].
- 801 Dickendeshler TL, Baldwin KT, Mironova YA, Koriyama Y, Raiker SJ, Askew KL, Wood A,
802 Geoffroy CG, Zheng B, Liepmann CD, Katagiri Y, Benowitz LI, Geller HM, Giger RJ
803 (2012) NgR1 and NgR3 are receptors for chondroitin sulfate proteoglycans. Nat
804 Neurosci 15:703–712 Available at:
805 [http://www.pubmedcentral.nih.gov/articlerender.fcgi?artid=3337880&tool=pmcentrez&](http://www.pubmedcentral.nih.gov/articlerender.fcgi?artid=3337880&tool=pmcentrez&rendertype=abstract)
806 [endertype=abstract](http://www.pubmedcentral.nih.gov/articlerender.fcgi?artid=3337880&tool=pmcentrez&rendertype=abstract) [Accessed August 6, 2014].
- 807 Fang J, Shaw PX, Wang Y, Goldberg JL (2016) Kru ppeL-Like Factor 4 (KLF4) Is Not
808 Required for Retinal Cell Differentiation. eNeuro 3 Available at:
809 <http://www.ncbi.nlm.nih.gov/pubmed/27022622> [Accessed February 1, 2017].
- 810 Gaudet AD, Mandrekar-Colucci S, Hall JCE, Sweet DR, Schmitt PJ, Xu X, Guan Z, Mo X,
811 Guerau-de-Arellano M, Popovich PG (2016) miR-155 Deletion in Mice Overcomes
812 Neuron-Intrinsic and Neuron-Extrinsic Barriers to Spinal Cord Repair. J Neurosci
813 36:8516–8532 Available at: <http://www.ncbi.nlm.nih.gov/pubmed/27511021> [Accessed
814 February 1, 2017].
- 815 Hancock ML, Preitner N, Quan J, Flanagan JG (2014) MicroRNA-132 is enriched in
816 developing axons, locally regulates Rasa1 mRNA, and promotes axon extension. J
817 Neurosci 34:66–78 Available at:
818 <http://www.jneurosci.org/cgi/doi/10.1523/JNEUROSCI.3371-13.2014> [Accessed
819 February 1, 2017].
- 820 He Z, Jin Y (2016) Intrinsic Control of Axon Regeneration. Neuron 90:437–451 Available at:
821 <http://www.ncbi.nlm.nih.gov/pubmed/27151637> [Accessed January 27, 2017].

- 822 Hu Y-W, Jiang J-J, Yan-Gao, Wang R-Y, Tu G-J (2016) MicroRNA-210 promotes sensory
823 axon regeneration of adult mice in vivo and in vitro. *Neurosci Lett* 622:61–66 Available
824 at: <http://www.ncbi.nlm.nih.gov/pubmed/27102143> [Accessed February 1, 2017].
- 825 Hu Z, Yu D, Gu Q, Yang Y, Tu K, Zhu J, Li Z (2014) miR-191 and miR-135 are required for
826 long-lasting spine remodelling associated with synaptic long-term depression. *Nat*
827 *Commun* 5:3263 Available at: <http://www.nature.com/doi/10.1038/ncomms4263>
828 [Accessed February 1, 2017].
- 829 Issler O, Haramati S, Paul ED, Maeno H, Navon I, Zwang R, Gil S, Mayberg HS, Dunlop
830 BW, Menke A, Awatramani R, Binder EB, Deneris ES, Lowry CA, Chen A (2014)
831 MicroRNA 135 is essential for chronic stress resiliency, antidepressant efficacy, and
832 intact serotonergic activity. *Neuron* 83:344–360 Available at:
833 <http://linkinghub.elsevier.com/retrieve/pii/S0896627314004863> [Accessed February 1,
834 2017].
- 835 Jiang J-J, Liu C-M, Zhang B-Y, Wang X-W, Zhang M, Saijilafu, Zhang S-R, Hall P, Hu Y-
836 W, Zhou F-Q (2015) MicroRNA-26a supports mammalian axon regeneration in vivo by
837 suppressing GSK3 β expression. *Cell Death Dis* 6:e1865 Available at:
838 <http://www.ncbi.nlm.nih.gov/pubmed/26313916> [Accessed February 1, 2017].
- 839 Kan AA, van Erp S, Derijck AAHA, de Wit M, Hessel EVS, O’Duibhir E, de Jager W, Van
840 Rijen PC, Gosselaar PH, de Graan PNE, Pasterkamp RJ (2012) Genome-wide
841 microRNA profiling of human temporal lobe epilepsy identifies modulators of the
842 immune response. *Cell Mol Life Sci* 69:3127–3145 Available at:
843 <http://www.ncbi.nlm.nih.gov/pubmed/22535415> [Accessed February 1, 2017].
- 844 Khatri R, Subramanian S (2013) MicroRNA-135b and Its Circuitry Networks as Potential
845 Therapeutic Targets in Colon Cancer. *Front Oncol* 3:268 Available at:
846 <http://journal.frontiersin.org/article/10.3389/fonc.2013.00268/abstract> [Accessed

- 847 February 1, 2017].
- 848 Lagos-Quintana M, Rauhut R, Lendeckel W, Tuschl T (2001) Identification of Novel Genes
849 Coding for Small Expressed RNAs. *Science* (80-) 294:853–858 Available at:
850 <http://www.ncbi.nlm.nih.gov/pubmed/11679670> [Accessed January 27, 2017].
- 851 Lagos-Quintana M, Rauhut R, Yalcin A, Meyer J, Lendeckel W, Tuschl T (2002)
852 Identification of tissue-specific microRNAs from mouse. *Curr Biol* 12:735–739
853 Available at: <http://www.ncbi.nlm.nih.gov/pubmed/12007417> [Accessed February 1,
854 2017].
- 855 Li P, Teng Z-Q, Liu C-M (2016) Extrinsic and Intrinsic Regulation of Axon Regeneration by
856 MicroRNAs after Spinal Cord Injury. *Neural Plast* 2016:1–11 Available at:
857 <http://www.ncbi.nlm.nih.gov/pubmed/27818801> [Accessed February 1, 2017].
- 858 Lin C-W, Chang Y-L, Chang Y-C, Lin J-C, Chen C-C, Pan S-H, Wu C-T, Chen H-Y, Yang
859 S-C, Hong T-M, Yang P-C (2013) MicroRNA-135b promotes lung cancer metastasis by
860 regulating multiple targets in the Hippo pathway and LZTS1. *Nat Commun* 4:1877
861 Available at: <http://www.nature.com/doi/10.1038/ncomms2876> [Accessed
862 February 1, 2017].
- 863 Lin L, He Y, Xi B-L, Zheng H-C, Chen Q, Li J, Hu Y, Ye M-H, Chen P, Qu Y (2016) MiR-
864 135a Suppresses Calcification in Senescent VSMCs by Regulating KLF4/STAT3
865 Pathway. *Curr Vasc Pharmacol* 14:211–218 Available at:
866 <http://www.ncbi.nlm.nih.gov/pubmed/26202084> [Accessed February 1, 2017].
- 867 Martirosyan NL, Carotenuto A, Patel AA, Kalani MYS, Yagmurlu K, Lemole GM, Preul
868 MC, Theodore N (2016) The Role of microRNA Markers in the Diagnosis, Treatment,
869 and Outcome Prediction of Spinal Cord Injury. *Front Surg* 3:56 Available at:
870 <http://www.ncbi.nlm.nih.gov/pubmed/27878119> [Accessed February 1, 2017].
- 871 Moore DL, Blackmore MG, Hu Y, Kaestner KH, Bixby JL, Lemmon VP, Goldberg JL (2009)

- 872 KLF family members regulate intrinsic axon regeneration ability. *Science* 326:298–301
873 Available at: <http://www.sciencemag.org/cgi/doi/10.1126/science.1175737> [Accessed
874 February 1, 2017].
- 875 Moritoki Y, Hayashi Y, Mizuno K, Kamisawa H, Nishio H, Kurokawa S, Ugawa S, Kojima
876 Y, Kohri K (2014) Expression profiling of microRNA in cryptorchid testes: miR-135a
877 contributes to the maintenance of spermatogonial stem cells by regulating FoxO1. *J Urol*
878 191:1174–1180 Available at:
879 <http://linkinghub.elsevier.com/retrieve/pii/S002253471305876X> [Accessed February 1,
880 2017].
- 881 Nagel R, le Sage C, Diosdado B, van der Waal M, Oude Vrielink JAF, Bolijn A, Meijer GA,
882 Agami R (2008) Regulation of the adenomatous polyposis coli gene by the miR-135
883 family in colorectal cancer. *Cancer Res* 68:5795–5802 Available at:
884 <http://cancerres.aacrjournals.org/cgi/doi/10.1158/0008-5472.CAN-08-0951> [Accessed
885 February 1, 2017].
- 886 Phay M, Kim HH, Yoo S (2015) Dynamic Change and Target Prediction of Axon-Specific
887 MicroRNAs in Regenerating Sciatic Nerve Di Giovanni S, ed. *PLoS One* 10:e0137461
888 Available at: <http://www.ncbi.nlm.nih.gov/pubmed/26331719> [Accessed February 1,
889 2017].
- 890 Poell JB, van Haastert RJ, Cerisoli F, Bolijn AS, Timmer LM, Diosdado-Calvo B, Meijer GA,
891 van Puijenbroek AAFL, Berezikov E, Schaapveld RQJ, Cuppen E (2011) Functional
892 microRNA screening using a comprehensive lentiviral human microRNA expression
893 library. *BMC Genomics* 12:546 Available at:
894 <http://bmcgenomics.biomedcentral.com/articles/10.1186/1471-2164-12-546> [Accessed
895 February 1, 2017].
- 896 Qin S, Liu M, Niu W, Zhang C-L (2011) Dysregulation of Kruppel-like factor 4 during brain

- 897 development leads to hydrocephalus in mice. *Proc Natl Acad Sci* 108:21117–21121
898 Available at: <http://www.ncbi.nlm.nih.gov/pubmed/22160720> [Accessed February 1,
899 2017].
- 900 Qin S, Zhang C-L (2012) Role of Kruppel-like factor 4 in neurogenesis and radial neuronal
901 migration in the developing cerebral cortex. *Mol Cell Biol* 32:4297–4305 Available at:
902 <http://mcb.asm.org/cgi/doi/10.1128/MCB.00838-12> [Accessed February 1, 2017].
- 903 Qin S, Zou Y, Zhang C-L (2013) Cross-talk between KLF4 and STAT3 regulates axon
904 regeneration. *Nat Commun* 4:2633 Available at:
905 <http://www.ncbi.nlm.nih.gov/pubmed/24129709> [Accessed February 1, 2017].
- 906 Ren J-W, Li Z-J, Tu C (2015) MiR-135 post-transcriptionally regulates FOXO1 expression
907 and promotes cell proliferation in human malignant melanoma cells. *Int J Clin Exp*
908 *Pathol* 8:6356–6366 Available at: <http://www.ncbi.nlm.nih.gov/pubmed/26261511>
909 [Accessed February 1, 2017].
- 910 Rossi M, Kilpinen H, Muona M, Surakka I, Ingle C, Lahtinen J, Hennah W, Ripatti S,
911 Hovatta I (2014) Allele-specific regulation of DISC1 expression by miR-135b-5p. *Eur J*
912 *Hum Genet* 22:840–843 Available at:
913 <http://www.nature.com/doi/10.1038/ejhg.2013.246> [Accessed February 1, 2017].
- 914 Sempere LF, Freemantle S, Pitha-Rowe I, Moss E, Dmitrovsky E, Ambros V (2004)
915 Expression profiling of mammalian microRNAs uncovers a subset of brain-expressed
916 microRNAs with possible roles in murine and human neuronal differentiation. *Genome*
917 *Biol* 5:R13 Available at: <http://genomebiology.biomedcentral.com/articles/10.1186/gb-2004-5-3-r13> [Accessed February 1, 2017].
- 919 Shi H, Ji Y, Zhang D, Liu Y, Fang P (2015) MiR-135a inhibits migration and invasion and
920 regulates EMT-related marker genes by targeting KLF8 in lung cancer cells. *Biochem*
921 *Biophys Res Commun* 465:125–130 Available at:

- 922 <http://linkinghub.elsevier.com/retrieve/pii/S0006291X15303466> [Accessed February 1,
923 2017].
- 924 Song Y, Ori-McKenney KM, Zheng Y, Han C, Jan LY, Jan YN (2012) Regeneration of
925 *Drosophila* sensory neuron axons and dendrites is regulated by the Akt pathway
926 involving Pten and microRNA bantam. *Genes Dev* 26:1612–1625 Available at:
927 <http://www.ncbi.nlm.nih.gov/pubmed/22759636> [Accessed February 1, 2017].
- 928 Steketee MB, Oboudiyat C, Daneman R, Trakhtenberg E, Lamoureux P, Weinstein JE,
929 Heidemann S, Barres BA, Goldberg JL (2014) Regulation of Intrinsic Axon Growth
930 Ability at Retinal Ganglion Cell Growth Cones. *Investig Ophthalmology Vis Sci* 55:4369
931 Available at: <http://iovs.arvojournals.org/article.aspx?doi=10.1167/iovs.14-13882>
932 [Accessed February 1, 2017].
- 933 Valeri N et al. (2014) MicroRNA-135b promotes cancer progression by acting as a
934 downstream effector of oncogenic pathways in colon cancer. *Cancer Cell* 25:469–483
935 Available at: <http://linkinghub.elsevier.com/retrieve/pii/S1535610814001159> [Accessed
936 February 1, 2017].
- 937 Van Battum EY, Gunput R-AF, Lemstra S, Groen EJN, Yu K Lou, Adolfs Y, Zhou Y,
938 Hoogenraad CC, Yoshida Y, Schachner M, Akhmanova A, Pasterkamp RJ (2014) The
939 intracellular redox protein MICAL-1 regulates the development of hippocampal mossy
940 fibre connections. *Nat Commun* 5:4317 Available at:
941 <http://www.ncbi.nlm.nih.gov/pubmed/25007825> [Accessed July 14, 2014].
- 942 van Erp S, van den Heuvel DMA, Fujita Y, Robinson RA, Hellemons AJCGM, Adolfs Y,
943 Van Battum EY, Blokhuis AM, Kuijpers M, Demmers JAA, Hedman H, Hoogenraad
944 CC, Siebold C, Yamashita T, Pasterkamp RJ (2015) Lrig2 Negatively Regulates
945 Ectodomain Shedding of Axon Guidance Receptors by ADAM Proteases. *Dev Cell*
946 35:537–552 Available at: <http://www.ncbi.nlm.nih.gov/pubmed/26651291> [Accessed

- 947 April 29, 2016].
- 948 Weitz AC, Behrend MR, Lee NS, Klein RL, Chiodo VA, Hauswirth WW, Humayun MS,
949 Weiland JD, Chow RH (2013) Imaging the response of the retina to electrical
950 stimulation with genetically encoded calcium indicators. *J Neurophysiol* 109:1979–1988
951 Available at: <http://www.ncbi.nlm.nih.gov/pubmed/23343890> [Accessed August 7,
952 2017].
- 953 Wu CW, Ng SC, Dong Y, Tian L, Ng SSM, Leung WW, Law WT, Yau TO, Chan FKL, Sung
954 JJY, Yu J (2014) Identification of microRNA-135b in Stool as a Potential Noninvasive
955 Biomarker for Colorectal Cancer and Adenoma. *Clin Cancer Res* 20:2994–3002
956 Available at: <http://www.ncbi.nlm.nih.gov/pubmed/24691020> [Accessed February 1,
957 2017].
- 958 Wu D, Raafat A, Pak E, Clemens S, Murashov AK (2012) Dicer-microRNA pathway is
959 critical for peripheral nerve regeneration and functional recovery in vivo and
960 regenerative axonogenesis in vitro. *Exp Neurol* 233:555–565 Available at:
961 <http://linkinghub.elsevier.com/retrieve/pii/S0014488611004456> [Accessed February 1,
962 2017].
- 963 Xiao F, Zuo Z, Cai G, Kang S, Gao X, Li T (2009) miRecords: an integrated resource for
964 microRNA-target interactions. *Nucleic Acids Res* 37:D105-10 Available at:
965 <https://academic.oup.com/nar/article-lookup/doi/10.1093/nar/gkn851> [Accessed
966 February 1, 2017].
- 967 Yang X, Wang X, Nie F, Liu T, Yu X, Wang H, Li Q, Peng R, Mao Z, Zhou Q, Li G (2015)
968 miR-135 family members mediate podocyte injury through the activation of Wnt/ β -
969 catenin signaling. *Int J Mol Med* Available at: [http://www.spandidos-
970 publications.com/10.3892/ijmm.2015.2259](http://www.spandidos-publications.com/10.3892/ijmm.2015.2259) [Accessed February 1, 2017].
- 971 Yao S, Tian C, Ding Y, Ye Q, Gao Y, Yang N, Li Q (2016) Down-regulation of Krüppel-like

972 factor-4 by microRNA-135a-5p promotes proliferation and metastasis in hepatocellular
973 carcinoma by transforming growth factor- β 1. *Oncotarget* 7:42566–42578 Available at:
974 <http://www.oncotarget.com/abstract/9934> [Accessed February 1, 2017].

975 Yau KW, van Beuningen SFB, Cunha-Ferreira I, Cloin BMC, van Battum EY, Will L,
976 Schätzle P, Tas RP, van Krugten J, Katrukha EA, Jiang K, Wulf PS, Mikhaylova M,
977 Harterink M, Pasterkamp RJ, Akhmanova A, Kapitein LC, Hoogenraad CC (2014)
978 Microtubule minus-end binding protein CAMSAP2 controls axon specification and
979 dendrite development. *Neuron* 82:1058–1073 Available at:
980 <http://linkinghub.elsevier.com/retrieve/pii/S089662731400333X> [Accessed February 1,
981 2017].

982 Zhang YK, Sun B, Sui G (2016) Serum microRNA-135a downregulation as a prognostic
983 marker of non-small cell lung cancer. *Genet Mol Res* 15 Available at:
984 <http://www.ncbi.nlm.nih.gov/pubmed/27525941> [Accessed February 1, 2017].

985 Ziats MN, Rennert OM (2014) Identification of differentially expressed microRNAs across
986 the developing human brain. *Mol Psychiatry* 19:848–852 Available at:
987 <http://www.nature.com/doi/10.1038/mp.2013.93> [Accessed February 1, 2017].

988 Zou Y, Chiu H, Zinovyeva A, Ambros V, Chuang C-F, Chang C (2013) Developmental
989 Decline in Neuronal Regeneration by the Progressive Change of Two Intrinsic Timers.
990 *Science* (80-) 340:372–376 Available at:
991 <http://www.ncbi.nlm.nih.gov/pubmed/23599497> [Accessed February 1, 2017].
992
993

994 **Figure legends**

995

996 **Figure 1.** Image-based high content screen identifies miRNAs involved in neurite growth.

997 (A) Schematic representation of the Cellomics ArrayScan screen. SH-SY5Y cells were seeded
998 and differentiated using retinoic acid. Viral library was added and after 3 days cells were
999 fixed and immunostained. Images covering the entire surface of the well were taken using a
1000 Thermo Arrayscan automated microscope and analyzed using a Neuronal Profiling algorithm
1001 to assess the effect of miRNAs on general neuron-like features, such as the number of
1002 neurites, neurite length, and number of branch-points. The effect of a miRNA on each
1003 parameter was scored binarily (0 or 1). A positive score (1) was given when the effect on the
1004 parameter deviated more than 2 times the standard deviation of the median value for all
1005 miRNAs. Scores for each of the triplicate plates were combined, with the score for a certain
1006 parameter taken into account (effect is ‘true’) when the miRNA scored positive in a minimum
1007 of 2 out of 3 plates. This resulted in a final (cumulative) ‘hitscore’ which was used to rank the
1008 lentiviral clones for an effect on neuronal morphology.

1009 (B) Representative images of untreated SH-SY5Y cells (left panel) and SH-SY5Y cells
1010 treated with retinoic acid (middle panel). The right panel shows the result of tracings
1011 generated by the Neuronal Profiling algorithm. Scale bar: 100 μm .

1012 (C) Graph showing the cumulative score of all the parameters of the Neuronal Profiling
1013 algorithm for the top list of annotated miRNAs that have a positive effect on neuronal features
1014 of virus-transduced SH-SY5Y cells.

1015 (D) Sequence and genomic location of miR-135a and miR-135b. The mature sequence of
1016 miR-135a and miR-135b differs by only one nucleotide (underlined) outside the seed region
1017 (in red).

1018 (E) Graphs showing average total hitscore (left), hitscore based on parameters describing
1019 neurite length (middle), and hitscore based on parameters describing neurite branching (right)
1020 of SH-SY5Y cells electroporated with the indicated miRIDIAN miRNA mimics. Data are
1021 expressed as means \pm SEM. * $p < 0.05$, ** $p < 0.01$, *** $p < 0.001$, **** $p < 0.0001$, One-
1022 way ANOVA with Tukeys multiple comparison test. Scale bar: 200 μ m.

1023

1024 **Figure 2.** Expression of miR-135a and miR-135b during neuronal development.

1025 (A, C) Graphs show results of quantitative PCR experiments on RNA from isolated mouse
1026 cortex (A) or hippocampus (C) from 5 different embryonic and post-natal stages. Tissue from
1027 three different mice from different litters was used for analysis. Samples were run in
1028 duplicate. Fold changes are relative to 5S housekeeping rRNA expression. Data are expressed
1029 as means \pm SEM.

1030 (B) Locked-nucleic acid (LNA) *in situ* hybridization shows miR-135a and miR-135b
1031 expression in the E14, P10 and adult cortex. miR-135a and miR-135b are expressed in the
1032 cortical plate (cp) and upper layers of the adult cortex. Sections treated with scrambled LNA-
1033 *in situ* probes were devoid of specific staining. Scale bars: 200 μ m.

1034 (D) Locked-nucleic acid (LNA) *in situ* hybridization shows miR-135a and miR-135b
1035 expression in the E16, P0, P10 and adult hippocampus. In the hippocampus, the dentate gyrus
1036 (DG) and CA3 region specifically show strong miR-135a and miR-135b staining. Sections
1037 treated with scrambled LNA-*in situ* probes were devoid of specific staining. Scale bars: 200
1038 μ m.

1039

1040 **Figure 3.** miR-135a and miR-135b increase neurite outgrowth and branching.

1041 (A) Graphs show results of quantitative PCR on primary hippocampal neurons at different
1042 days in vitro (DIV). RNA was collected from 3-4 coverslips of two different cultures.

1043 Samples were run in duplicate. Fold changes are relative to 5S housekeeping rRNA
1044 expression. Data are expressed as means \pm SEM.

1045 (B) Representative silhouettes of primary neurons at day *in vitro* (DIV) 4 following
1046 transfection with control-1, miR-135a, miR-135b and miR-135a/miR-135b mimics. Longest
1047 neurites are labelled in green.

1048 (C) Graph shows results of tracing of the longest neurite of DIV4 hippocampal neurons in
1049 experiments as in A. At least 173 neurons were traced from ≥ 3 individual experiments. Data
1050 are expressed as means \pm SEM. ** $p < 0.01$, **** $p < 0.0001$, T-test.

1051 (D) Quantification of tracing of the longest neurite of DIV4 hippocampal neurons after
1052 transfection with scrambled or miR-135a and miR-135b H1-mCherry-sponge vectors. At least
1053 100 neurons were traced from ≥ 3 individual experiments. Data are expressed as means \pm
1054 SEM. ** $p < 0.01$, T-test.

1055 (E) Representative silhouettes of primary neurons at DIV 4 following transfection with
1056 control sponge - or miR-135ab sponge vector. Longest neurites are labelled in green.

1057 (F) Sholl analysis from 31 control-1 (grey), 15 miR-135a (green), 16 miR-135b (blue) or 23
1058 miR-135a and miR-135b (red) over-expressing neurons reveals increased branching in
1059 proximal neurites and in the distal axon. Data are expressed as means \pm SEM. **** $p <$
1060 0.0001, multiple T-tests. In the silhouette, proximal neurites are marked in blue, and distal
1061 branches are marked in red.

1062 (G) Cumulative intersections of neurites from neurons transfected with control-1 or miR-135a
1063 and miR-135b mimics with the sholl-circles (as in D). Data are expressed as means \pm SEM.
1064 ** $p < 0.01$, T-test.

1065

1066 **Figure 4.** miR-135s are required for cortical neuron migration.

1067 (A) Representative images of cortices that were *ex vivo* electroporated with control-1, miR-
1068 135a, or miR-135b mimics. Neuron migration was quantified by placing a rectangle
1069 containing 8 square bins perpendicular on the cortex. Cells in each bin were counted and
1070 expressed as percentage of the total number of cells in the rectangle. The bins perfectly align
1071 with the layers of the cortex: ventricular zone (vz), subventricular zone (svz), intermediate
1072 zone (iz), cortical plate (cp), and marginal zone (mz). Cell-counts of two to three rectangles
1073 per section were used for comparison. At least two to three sections from ≥ 3 animals from
1074 different litters were used. Data are expressed as means \pm SEM. Red** bin7 control-1 vs.
1075 miR-135a: MWU = 24, $p = 0.0042$; blue* bin 4 control-1 vs. miR-135b: MWU = 32, $p =$
1076 0.0195 ; blue** bin 7 control-1 vs. miR-135b: MWU = 25, $p = 0.0051$, Mann-Whitney U tests.
1077 Scale bar: 100 μm .

1078 (B) Representative images and quantification of neuron migration and leading process length
1079 in *in utero* electroporated E16.5 cortices of mice embryos treated with either control-1 or
1080 miR-135a and miR-135b mimics. GFP signal in white. Neuron migration was quantified as
1081 described in (F). Data are expressed as means \pm SEM. Bin 3: MWU = 198, $p < 0.0001$; bin6
1082 MWU = 282, $p < 0.0053$; bin 7: MWU = 161, $p < 0.0001$; bin 8: MWU = 164, $p < 0.0001$. **
1083 $p < 0.01$, **** $p < 0.0001$, Mann-Whitney U tests, **** $p < 0.0001$ T-test. Scale bar: 100 μm .

1084 (C) Representative images and quantification of neuron migration and leading process length
1085 in *in utero* electroporated E16.5 cortices of mice embryos treated with either scrambled or
1086 miR-135a and miR-135b H1-mCherry-sponge vectors. mCherry signal in white. Neuron
1087 migration was quantified as described in (A). Data are expressed as means \pm SEM. Bin 2:
1088 MWU = 70, $p = 0.018$; bin 5: MWU = 69, $p = 0.016$; bin 6: MWU = 75, $p = 0.030$; bin 8:
1089 MWU = 69, $p = 0.016$, Mann-Whitney U tests, * $p < 0.05$. **** $p < 0.0001$ T-test. Scale bar:
1090 100 μm .

1091 (D) Representative images and quantification of neuron migration in *in utero* electroporated
1092 P4 cortices of mice pups electroporated with either control-1 or miR-135a and miR-135b
1093 mimics at E14.5. GFP signal in white. Neuron migration was quantified as described in (A).
1094 Data are expressed as means \pm SEM. Bin3: MWU = 475, $p = 0.0114$; bin 4: MWU = 392.5, p
1095 = 0.0016; bin 5: MWU = 148, $p < 0.0001$; bin 6: MWU = 319.5, $p = 0.0004$; bin 7: MWU =
1096 194.5, $p < 0.0001$, Mann-Whitney U tests. * $p < 0.05$, ** $p < 0.01$, *** $p < 0.001$, **** $p <$
1097 0.0001. Scale bar: 200 μm .

1098 (E) Representative images and quantification of neuron migration in *in utero* electroporated
1099 P10 cortices of mice pups electroporated with either control-1 or miR-135a and miR-135b
1100 mimics at E14.5. GFP signal in white. Neuron migration was quantified as described in (A).
1101 Data are expressed as means \pm SEM. Bin 6: MWU 783.5, $p = 0.032$, Mann-Whitney U test. *
1102 $p < 0.05$. Scale bar: 200 μm .

1103

1104 **Figure 5.** Krüppel-like factor 4 (KLF4) is a functional target for miR-135a and miR-135b
1105 during axonal development and neuron migration.

1106 (A) Schematic representation of predicted miR-135a and miR-135b binding sites in the 3'-
1107 UTR of KLF4 mRNA. Site 394 is predicted to mediate strongest binding (marked by arrow).

1108 (B) The 3'-UTR of KLF4 was cloned into a psi-CHECK2 vector and used for a renilla-
1109 luciferase assay with control-1 or miR-135a and miR-135b mimics. Subsequently, a psi-
1110 CHECK vector with the KLF4 3'-UTR in which 3 nucleotides within site 394 were mutated
1111 was used to confirm specificity of miRNA-135-KLF4 binding. Luciferase activity was
1112 normalized to the 3'-UTR only condition of either wild-type or mutated 3'-UTR (UTRm).
1113 The experiment was repeated 3 times. Data are expressed as means \pm SEM. ** $p < 0.01$, * $p <$
1114 0.05, T-test.

1115 (C) Immunohistochemistry of KLF4 in sections of mouse cortex and hippocampus at E16.5
1116 and adulthood. KLF4 is highly expressed in the cortical plate (cp), in axons running through
1117 the intermediate zone (iz) and in hippocampal granule cells in the dentate gyrus (DG) and in
1118 pyramidal cells of the CA3. Scale bars: 200 μm .

1119 (D) Western blot analysis of KLF4 protein levels after transfection of control-1 or miR-135a
1120 and miR-135b mimics in Neuro2A cells. Data are expressed as means \pm SEM. ** $p < 0.01$, T-
1121 test.

1122 (E) Representative silhouettes of primary hippocampal neurons at 4 days in vitro (DIV 4)
1123 after transfection with control-1 mimics, control-1 mimics combined with a KLF4 cDNA
1124 insensitive for miRNA binding (CMV-KLF4-GFP), miR-135a and miR-135b mimics, and
1125 miR-135a and miR-135b mimics combined with CMV-KLF4-GFP.

1126 (F) Graph shows results of tracing of the longest neurite of DIV4 hippocampal neurons in
1127 experiments as in E. At least 182 neurons were traced from ≥ 3 individual experiments. Data
1128 are expressed as means \pm SEM. * $p < 0.05$, *** $p < 0.001$, **** $p < 0.0001$, T-test.

1129 (G) Representative images and quantification of neuron migration and leading process length
1130 in *in utero* electroporated E16.5 cortices of mice embryos treated with either miR-135a and
1131 miR-135b mimics, or miR-135a and miR-135b mimics combined with a pCAG-KLF4 vector
1132 which is insensitive to miR-135 regulation. Neuron migration was quantified as described in
1133 Figure 4. Data are expressed as means \pm SEM. Bin1: MWU = 422, $p = 0.0171$, bin2: MWU =
1134 332, $p = 0.0005$, bin3: MWU = 293, $p < 0.0001$, bin4: MWU = 395, $p = 0.0068$, bin5: MWU
1135 = 357, $p = 0.0016$, bin6: MWU = 261, $p < 0.0001$, bin7: MWU = 219, $p < 0.0001$ and bin8:
1136 MWU = 211.5, $p < 0.0001$. Mann-Whitney U tests. * $p < 0.05$, ** $p < 0.01$, *** $p < 0.001$,
1137 **** $p < 0.0001$. Control-1 condition is as described in Figure 4B. Scale bar: 100 μm .

1138

1139 **Figure 6.** Exogenous miR-135s enhance axon regeneration after optic nerve injury.

1140 (A) Experimental setup of the optic nerve crush studies.

1141 (B, C) Graph shows results of quantitative PCR on eye tissue following injection of mimics.
1142 miR-135a and miR-135b levels are increased after two injections of miRNA-mimics, while
1143 KLF4 levels are decreased (C). Fold changes are relative to 5S housekeeping rRNA
1144 expression. Data are expressed as means \pm SEM. * $p < 0.05$, ** $p < 0.01$, T-test on delta Ct
1145 values.

1146 (D) Representative images of optic nerves stained for Cholera-toxin B conjugated to Alexa-
1147 555 14 days after optic nerve crush. Following injection of miR-135 mimics axons grow into
1148 and beyond the injury site (dotted lines indicate proximal and distal boundaries site of injury).
1149 Boxes indicate higher magnification images shown at the right. Scale bar: 100 μ m.

1150 (E) Graph shows quantification of the number of regenerating axons relative to the distal end
1151 of the crush site at 14 days post-injury for the conditions represented in (D). $n = 9$ mice per
1152 condition. * $p < 0.05$; **** $p < 0.0001$, ANOVA followed by Sidak's test. Data are presented
1153 as means \pm SEM.

1154 (F) Graph shows results of quantitative PCR on eye tissue following co-transfection of miR-
1155 135 mimics and GFP or KLF4 vector. No differences in miR-135a and miR-135b expression
1156 between the GFP or KLF4 transfected groups. Fold changes are relative to 5S housekeeping
1157 rRNA expression. Data are expressed as means \pm SEM.

1158 (G) AAV2-GFP virus was injected intravitreally. One week post-injection strong GFP signals
1159 are detected in RGCs but not in other cell types in the retina. Scale bar 100 μ m.

1160 (H) Graph shows quantification of the number of regenerating axons relative to the distal end
1161 of the crush site at 14 days post-injury for experiments performed using intravitreal injection
1162 of AAV2 (at 7 days post-lesion) expressing control miRNA or miR-135a and miR-135b (in
1163 addition to GFP). $n = 6$ mice per condition. **** $p < 0.0001$, ANOVA followed by Sidak's
1164 test. Data are presented as means \pm SEM.

1165 (I) Graph shows quantification of the number of regenerating axons relative to the distal end
1166 of the crush site at 14 days post-injury for experiments performed using intravitreal injection
1167 of control or miR-135a and miR-135b sponge vectors. $n = 6$ mice per condition. ** $p < 0.01$,
1168 ANOVA followed by Sidak's test. Data are presented as means \pm SEM.
1169

1170 **Table 1A.** Microscope settings and neuronal profiling algorithm parameters.
 1171

Image Acquisition		
Objective	10x	
Camera Name	ORCA-ER;1.00	
Acquisition Camera Mode	Standard (1024x1024;2x2)	
AutoFocus Camera Mode	AutoFocus (1024x1024;4x4)	
AutoFocus Field Interval	0	
Autofocus Parameters		
Fine Focus Step Size	17.6	
Fine Focus Plane Count	9	
Coarse Focus Step Size	70.4	
Coarse Focus Plane Count	9	
Smart Focus Plane Count	21	
Use Extended Range Focusing	False	
Apply Backlash Correction	False	
AutoFocus Method	STANDARD	
Use Relaxed Pass/Fail Criteria	False	
Focus Edge Threshold	0	
Focus Adjustment	0	
Focus Score Min Ratio	0.2	
Focus Score Mid Ratio	0.4	
Focus Score Max Ratio	0.5	
Focus Exposure Time for AutoExpose (seconds)	0.1	
Scan Limits		
Max Fields for Well	10	
Min Objects for Well	No Limit	
Max Sparse Fields for Well	No Limit	
Min Objects for Field	N/A	
Max Sparse Wells for Plate	N/A	
Channel 1: Nucleus		
Dye	XF100 - Hoechst	
Apply Illumination Correction	False	
Apply Background Correction	True	
Gain	25	
Use Apotome	False	
Z Offset	0.00	
Exposure Parameters (Ch 1)		
Method	Fixed	
Exposure Time (seconds)	0.495051	
Object Identification (Ch 1)		
Method	TriangleThreshold	
Value	0	
Object Selection Parameter	Min	Max
NucAreaCh1	50	400
NucShapeP2ACh1	0	1000
NucShapeLWRCh1	0	10
NucAvgIntenCh1	0	4095
NucTotalIntenCh1	0	10000000000
NucVarIntenCh1	0	32767
Display Options (Ch 1)		
Composite Color (Hex) #0000FF		
ValidNucleus #0000FF		
RejectedNucleus #FF7F00		

Channel 2: Neuronal		
Dye	XF100 - FITC (GFP)	
Apply Illumination Correction	False	
Apply Background Correction	True	
Gain	25	
Use Apotome	False	
Z Offset	0.00	
Exposure Parameters (Ch 2)		
Method	Fixed	
Exposure Time (seconds)	0.301046	
Object Identification (Ch 2)		
Method	IsodataThreshold	
Value	0	
Object Selection Parameter	Min	Max
NeuriteLengthCh2	10	100000
NeuriteWidthCh2	0	1000
NeuriteAvgIntenCh2	0	4095
NeuriteTotalIntenCh2	0	10000000000
CellBodyNucCountCh2	1	1
CellBodyAreaCh2	0	250000
CellBodyShapeP2ACh2	0	10
CellBodyShapeLWRCh2	0	10
CellBodyAvgIntenCh2	0	4095
CellBodyTotalIntenCh2	0	10000000000
Display Options (Ch 2)		
Composite Color (Hex) #00FF40		
Neurite #FF00FF		
Neurite __ #00FF00		
SelectedCellBody #0080FF		
RejectedCellBody #FF0000		
NeuritePoint #FFFF00		
Assay Algorithm NeuronalProfiling	V3.5	
Assay Version	6.2 (Local Version: 6.2.0.3519)	
Focus Channel	1	
#Channels	2	

1172
1173
1174

Table 1B. Assay parameters for hit score.

Assay Parameters	
UseReferenceWells	0
MinRefAvgNeuronCountPerField	1
UseMicrometers	0
PixelSize	1.29
Type_1_EventDefinition	90324.03
Type_2_EventDefinition	0
Type_3_EventDefinition	0
NucTypeCh1	0
BackgroundCorrectionCh1	-1
NucSmoothFactorCh1	0
RejectBorderNuCsCh1	1
CellBodyNucTotalAreaCh1LevelHigh	110
CellBodyNucTotalAreaCh1LevelHigh_CC	1
CellBodyNucTotalIntenCh1LevelHigh	80000
CellBodyNucTotalIntenCh1LevelHigh_CC	1

CellBodyNucAvgIntenCh1LevelHigh	850
CellBodyNucAvgIntenCh1LevelHigh_CC	1
MinCellBodyNucOverlapCh2	0
CellBodyAndNeuriteTypeCh2	0
BackgroundCorrectionCh2	0
CellBodySmoothFactorCh2	0
CellBodyDemarcationCh2	2
UseNucForCellBodySegmentationCh2	2
CellBodyMaskModifierCh2	1
RejectBorderCellBodiesCh2	1
NeuriteSmoothFactorCh2	1
NeuriteIdentificationModifierCh2	-0.97
NeuriteDetectRadiusCh2	3
NeuriteDetectMethodCh2	4
NeuriteDirectionCh2	3
NeuritePointResolutionCh2	1
NeuritePointDisplayModeCh2	2
RejectMultiplyTracedNeuritesCh2	0
UseCellBodyZOIForNeuriteTracingCh2	0
CellBodyNucCountCh2LevelHigh	1
CellBodyNucCountCh2LevelHigh_CC	1
CellBodyAreaCh2LevelHigh	340
CellBodyAreaCh2LevelHigh_CC	1
CellBodyShapeP2ACh2LevelHigh	1.3
CellBodyShapeP2ACh2LevelHigh_CC	1
CellBodyShapeLWRCh2LevelHigh	1.6
CellBodyShapeLWRCh2LevelHigh_CC	1
CellBodyTotalIntenCh2LevelHigh	150000
CellBodyTotalIntenCh2LevelHigh_CC	1
CellBodyAvgIntenCh2LevelHigh	650
CellBodyAvgIntenCh2LevelHigh_CC	1
NeuriteTotalCountCh2LevelHigh	3
NeuriteTotalCountCh2LevelHigh_CC	1
NeuriteTotalLengthCh2LevelHigh	20
NeuriteTotalLengthCh2LevelHigh_CC	1
NeuriteAvgLengthCh2LevelHigh	8
NeuriteAvgLengthCh2LevelHigh_CC	1
NeuriteMaxLengthWithBranchesCh2LevelHigh	10
NeuriteMaxLengthWithBranchesCh2LevelHigh_CC	1
NeuriteMaxLengthWithoutBranchesCh2LevelHigh	10
NeuriteMaxLengthWithoutBranchesCh2LevelHigh_CC	1
NeuriteTotalAreaCh2LevelHigh	60
NeuriteTotalAreaCh2LevelHigh_CC	1
NeuriteWidthCh2LevelHigh	3.57
NeuriteWidthCh2LevelHigh_CC	1
NeuriteTotalIntenCh2LevelHigh	8000
NeuriteTotalIntenCh2LevelHigh_CC	1
NeuriteAvgIntenCh2LevelHigh	200
NeuriteAvgIntenCh2LevelHigh_CC	1
NeuriteVarIntenCh2LevelHigh	125
NeuriteVarIntenCh2LevelHigh_CC	1
BranchPointTotalCountCh2LevelHigh	0.2
BranchPointTotalCountCh2LevelHigh_CC	1
BranchPointAvgCountCh2LevelHigh	0.1
BranchPointAvgCountCh2LevelHigh_CC	1

BranchPointCountPerNeuriteLengthCh2LevelHigh	0
BranchPointCountPerNeuriteLengthCh2LevelHigh_CC	1
BranchPointAvgDistFromCellBodyCh2LevelHigh	1
BranchPointAvgDistFromCellBodyCh2LevelHigh_CC	1
CrossPointTotalCountCh2LevelHigh	0.1
CrossPointTotalCountCh2LevelHigh_CC	1
CrossPointAvgCountCh2LevelHigh	0.1
CrossPointAvgCountCh2LevelHigh_CC	1
NucSegmentationCh1	4.1
CellBodySegmentationCh2	14.1

1175

1176

1177 Cellomics Arrayscan microscope settings (A) are described in the section ‘Image

1178 Acquisition’. Nuclear DAPI staining was detected in channel 1, whereas the cell body and

1179 neurites stained by β 3-tubulin were detected in channel 2. The Neuronal Profiling algorithm

1180 recognition parameters of the cells (B) are described in the sections ‘Channel 1: Nucleus’ and

1181 ‘Channel 2: Neuronal’. In the section ‘Assay Parameters’ parameters describing general

1182 neuron morphology, such as the number of neurites, neurite length, number of branch-points,

1183 are listed. The effect of each miRNA on these parameters was scored as described in the

1184 Experimental Procedures and Fig. 1A.

1185
1186

Table 2. Potential shared mRNA targets for miR-135a and miR-135b.

Refseq	Symbol	Description
NM_001127511	APC	Adenomatous polyposis coli (APC), transcript variant 1
NM_001002296	GOLGA7	golgi autoantigen, golgin subfamily a, 7
NM_001117	ADCYAP1	adenylate cyclase activating polypeptide 1 (pituitary)
NM_001156	ANXA7	annexin A7
NM_001186	BACH1	BTB and CNC homology 1, basic leucine zipper transcription factor 1
NM_002015	FOXO1	forkhead box O1
NM_002031	FRK	fyn-related kinase
NM_002267	KPNA3	karyopherin alpha 3 (importin alpha 4)
NM_002449	MSX2	msh homeobox 2
NM_003144	SSR1	signal sequence receptor, alpha (translocon-associated protein alpha)
NM_003145	SSR2	signal sequence receptor, beta (translocon-associated protein beta)
NM_003185	TAF4	TAF4 RNA polymerase II, TATA box binding protein (TBP)-associated factor, 135kDa
NM_003262	SEC62	SEC62 homolog (<i>S. cerevisiae</i>)
NM_003304	TRPC1	transient receptor potential cation channel, subfamily C, member 1
NM_004235	KLF4	Kruppel-like factor 4 (gut)
NM_004901	ENTPD4	ectonucleoside triphosphate diphosphohydrolase 4
NM_004972	JAK2	Janus kinase 2 (a protein tyrosine kinase)
NM_005124	NUP153	nucleoporin 153kDa
NM_005230	ELK3	ELK3, ETS-domain protein (SRF accessory protein 2)
NM_005569	LIMK2	LIM domain kinase 2
NM_005607	PTK2	PTK2 protein tyrosine kinase 2
NM_005813	PRKD3	protein kinase D3
NM_005907	MAN1A1	mannosidase, alpha, class 1A, member 1
NM_006066	AKR1A1	aldo-keto reductase family 1, member A1 (aldehyde reductase)
NM_006306	SMC1A	structural maintenance of chromosomes 1A
NM_006651	CPLX1	complexin 1
NM_007216	HPS5	Hermansky-Pudlak syndrome 5
NM_014573	TMEM97	transmembrane protein 97
NM_014790	JAKMIP2	janus kinase and microtubule interacting protein 2
NM_014918	CHSY1	chondroitin sulfate synthase 1
NM_014924	KIAA0831	KIAA0831
NM_016132	MYEF2	myelin expression factor 2
NM_016453	NCKIPSD	NCK interacting protein with SH3 domain
NM_017744	ST7L	suppression of tumorigenicity 7 like
NM_017770	ELOVL2	elongation of very long chain fatty acids (FEN1/Elo2, SUR4/Elo3, yeast)-like 2
NM_018951	HOXA10	homeobox A10
NM_019094	NUDT4	nudix (nucleoside diphosphate linked moiety X)-type motif 4
NM_021020	LZTS1	leucine zipper, putative tumor suppressor 1
NM_021255	PELI2	pellino homolog 2 (<i>Drosophila</i>)
NM_022484	TMEM168	transmembrane protein 168
NM_022731	NUCKS1	nuclear casein kinase and cyclin-dependent kinase substrate 1
NM_022758	C6orf106	chromosome 6 open reading frame 106
NM_032320	BTBD10	BTB (POZ) domain containing 10
NM_032804	ADO	2-aminoethanethiol (cysteamine) dioxygenase
NM_032995	ARHGEF4	Rho guanine nucleotide exchange factor (GEF) 4
NM_033427	CTTNBP2	cortactin binding protein 2
NM_138444	KCTD12	potassium channel tetramerisation domain containing 12
NM_145257	C1orf96	chromosome 1 open reading frame 96
NM_145735	ARHGEF7	Rho guanine nucleotide exchange factor (GEF) 7
NM_145753	PHLDB2	pleckstrin homology-like domain, family B, member 2

NM_152271	LONRF1	LON peptidase N-terminal domain and ring finger 1
NM_152520	ZNF385B	zinc finger protein 385B
NM_152758	YTHDF3	YTH domain family, member 3
NM_178496	C3orf59	chromosome 3 open reading frame 59
NM_178500	PHOSPHO1	phosphatase, orphan 1
NM_181054	HIF1A	hypoxia-inducible factor 1, alpha subunit (basic helix-loop-helix transcription factor)
NM_203350	ZRANB2	zinc finger, RAN-binding domain containing 2
NM_207346	TSEN54	tRNA splicing endonuclease 54 homolog (<i>S. cerevisiae</i>)

1187

1188 Predictions were made by the on-line bioinformatic tool miRecords. Within miRecords

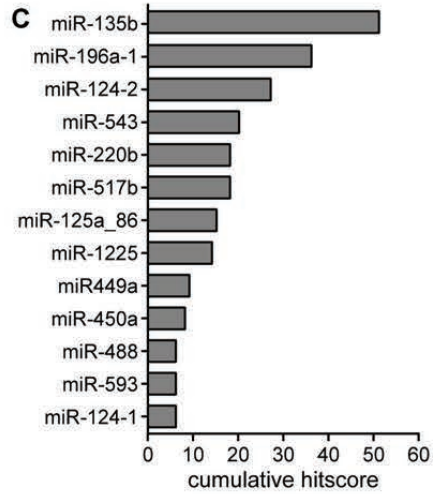
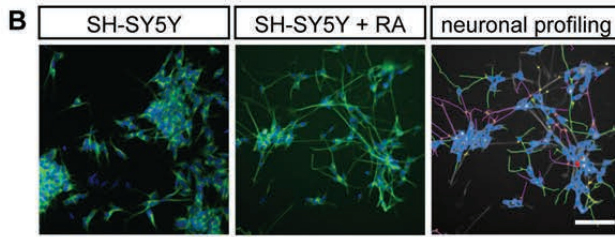
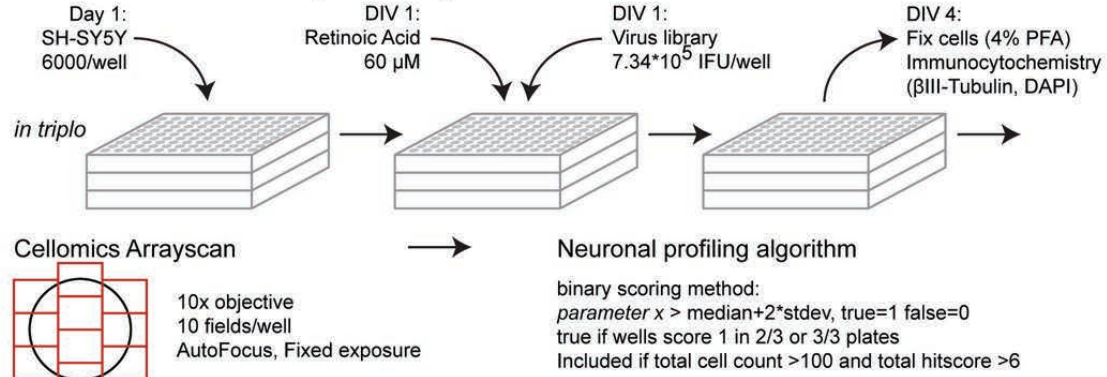
1189 targets were predicted using at least 6 different prediction programs: MiRanda, MirTarget2,

1190 PicTar, PITA, RNAhybrid, and TargetScan/TargetScanS.

1191

Figure 1

A Cell culture and immunocytochemistry



D

miR-135b	UAUGGCUUUUCAUUCUAUGUGA
	chr1: 205448302-205448398
miR-135a	UAUGGCUUUUUAUUCUAUGUGA
miR-135a-1	chr3: 52294219-52294308
miR-135a-2	chr12: 97563812-97563911

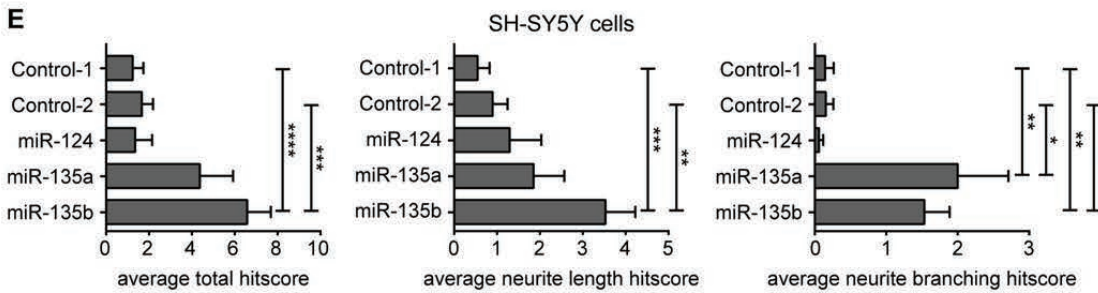


Figure 2

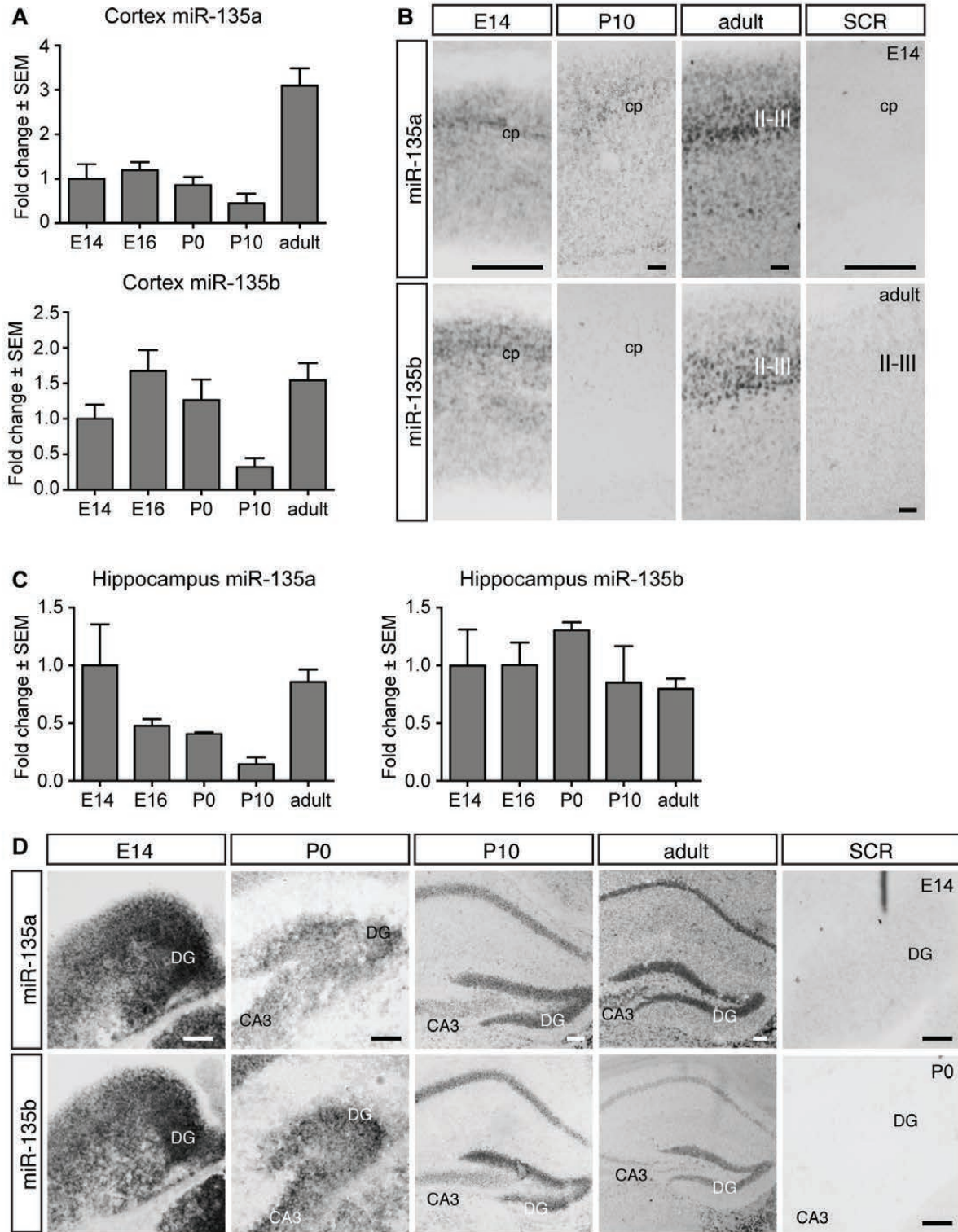


Figure 3

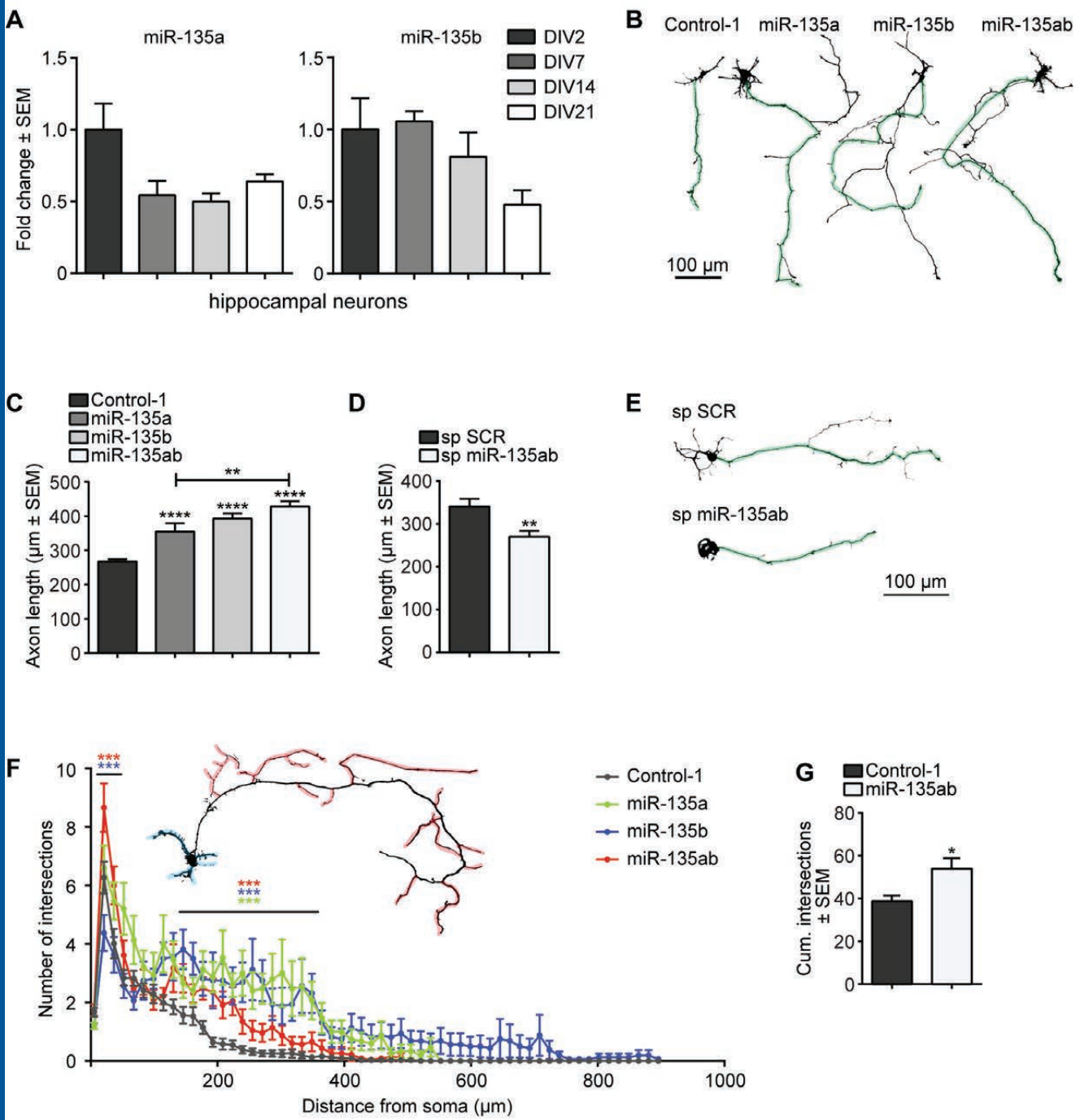


Figure 4

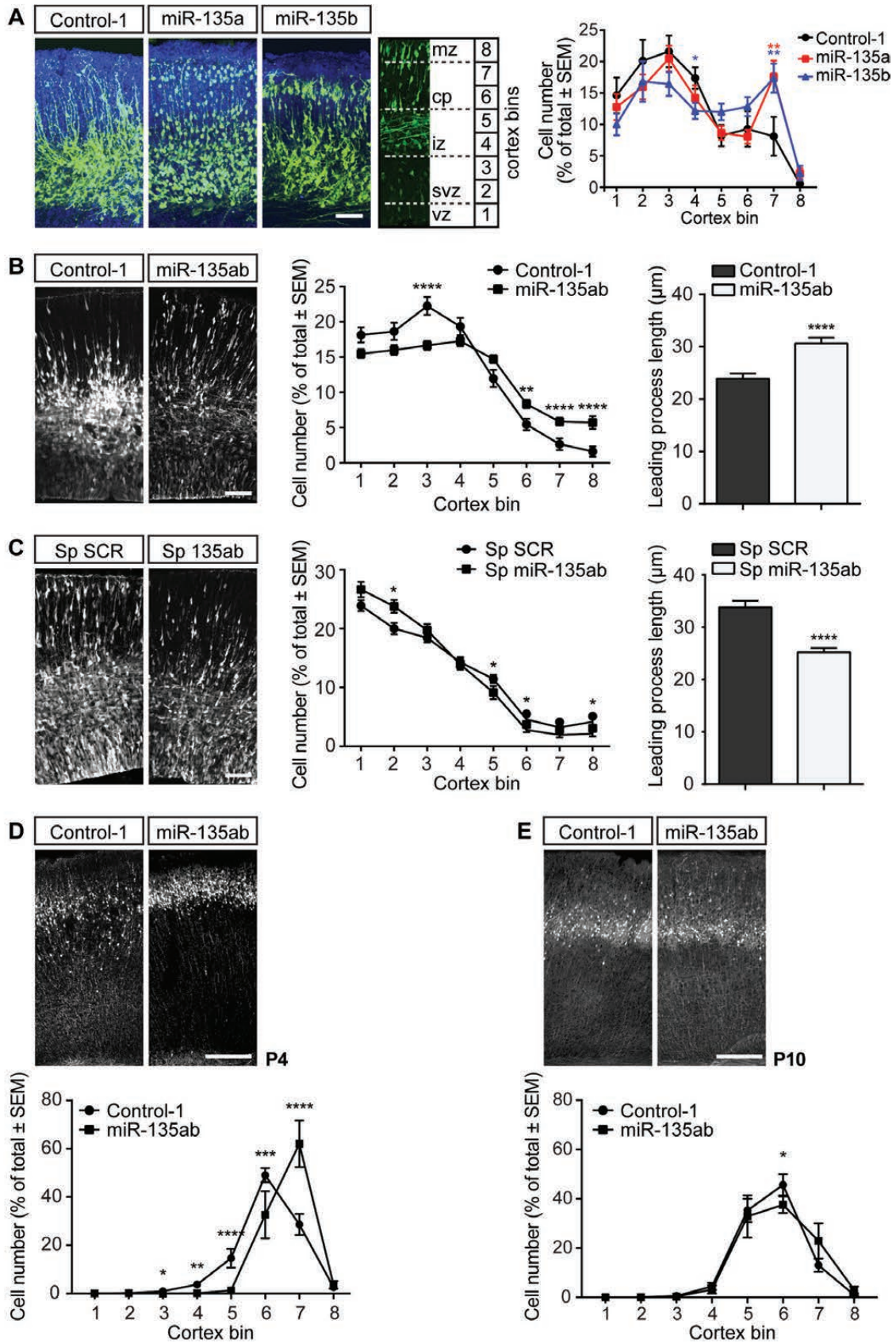
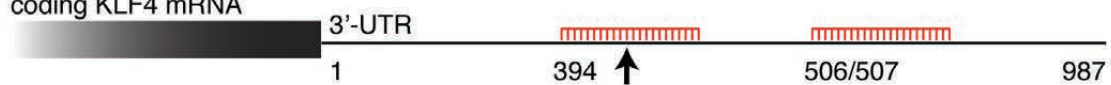
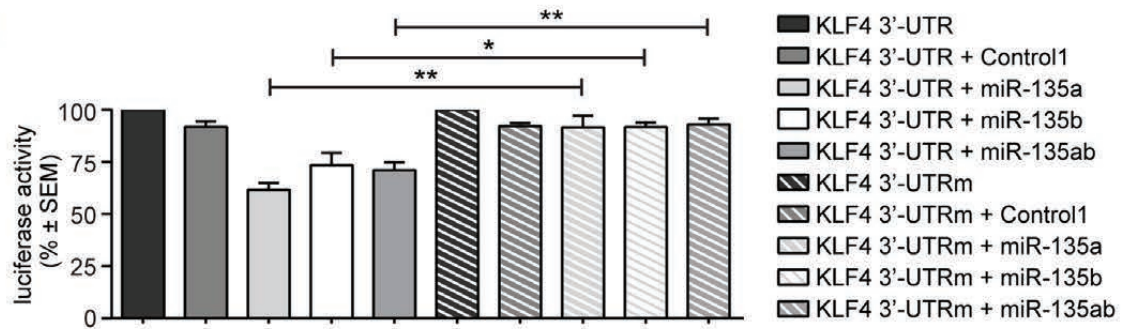


Figure 5

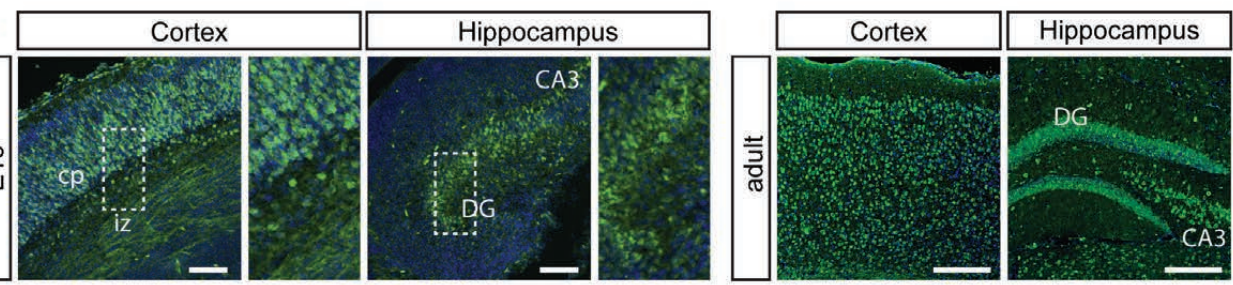
A coding KLF4 mRNA



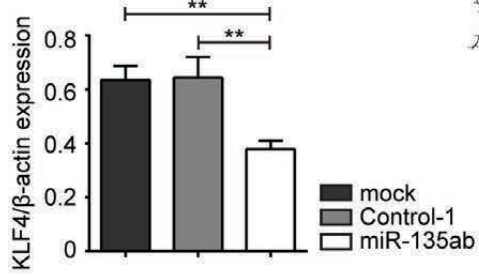
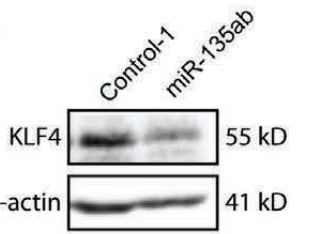
B



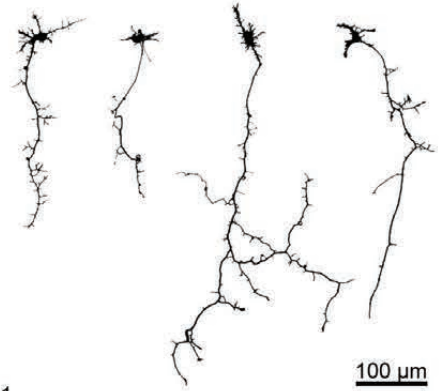
C



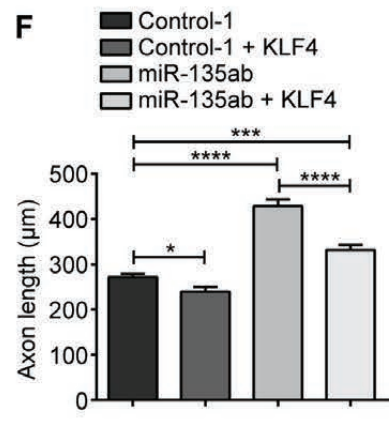
D



E Control-1 KLF4 miR-135ab 135ab + KLF4



F



G

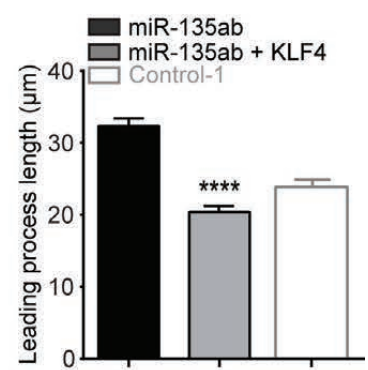
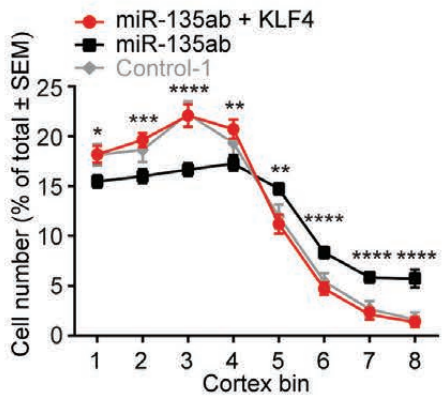
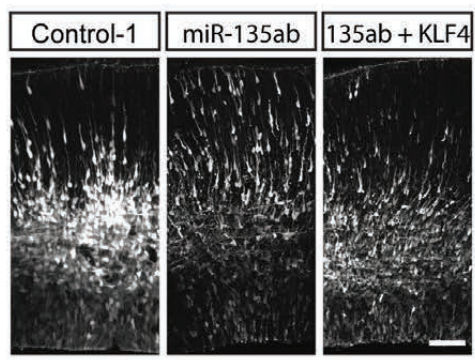


Figure 6

